

國 立 中 央 大 學

物 理 學 系
碩 士 論 文

Search for Pair Production of $t^* \rightarrow t + \gamma$:
Estimation of Photon Purity and Study of
the Top and W Mass Resolution

研 究 生：蔡 芳 英

指 導 教 授：余 欣 瑰

中 華 民 國 一 百 零 二 年 六 月



國立中央大學圖書館 碩博士論文電子檔授權書

(101年9月最新修正版)

本授權書授權本人撰寫之碩/博士學位論文全文電子檔(不包含紙本、詳備註1說明)，在「國立中央大學圖書館博碩士論文系統」。(以下請擇一勾選)

同意 (立即開放)

同意 (請於西元 _____ 年 _____ 月 _____ 日開放)

不同意，原因是：_____

在國家圖書館「臺灣博碩士論文知識加值系統」

同意 (立即開放)

同意 (請於西元 _____ 年 _____ 月 _____ 日開放)

不同意，原因是：_____

以非專屬、無償授權國立中央大學、台灣聯合大學系統圖書館與國家圖書館，基於推動「資源共享、互惠合作」之理念，於回饋社會與學術研究之目的，得不限地域、時間與次數，以紙本、微縮、光碟及其它各種方法將上列論文收錄、重製、與利用，並得將數位化之上列論文與論文電子檔以上載網路方式，提供讀者基於個人非營利性質之線上檢索、閱覽、下載或列印。

研究生簽名: 蔡芳英 蔡芳英 學號: 100222030

論文名稱: Search for Pair Production of t^* → t + γ : Estimation of Photon Purity and Study of the Top and W Mass Resolution

指導教授姓名: 余欣珊

系所 : 物理所 所 博士班 碩士班

備註：

1. 本授權書之授權範圍僅限電子檔，紙本論文部分依著作權法第 15 條第 3 款之規定，採推定原則即預設同意圖書館得公開上架閱覽，如您有申請專利或投稿等考量，不同意紙本上架陳列，須另行加填聲明書，詳細說明與紙本聲明書請至 <http://thesis.lib.ncu.edu.tw/> 下載。
2. 本授權書請填寫並親筆簽名後，裝訂於各紙本論文封面後之次頁（全文電子檔內之授權書簽名，可用電腦打字代替）。
3. 請加印一份單張之授權書，填寫並親筆簽名後，於辦理離校時交圖書館（以統一代轉寄給國家圖書館）。
4. 讀者基於個人非營利性質之線上檢索、閱覽、下載或列印上列論文，應遵守著作權法規定。

國立中央大學碩士班研究生
論文指導教授推薦書

物理 學系/研究所 蔡芳英 研究生所提之論
文 Search for pair production of $t^* \rightarrow t\gamma$
係由本人指導撰述，同意提付審查。

指導教授 余仁明 (簽章)

2013年6月17日

國立中央大學碩士班研究生

論文口試委員審定書

物理 學系/研究所 蔡芳英 研究生
所提之論文

Search for Pair Production of $t^* \rightarrow t + \gamma$: Estimation of Photon Purity
and Study of the Top and W Mass Resolution 經

本委員會審議，認定符合碩士資格標準。

學位考試委員會召集人

張元翰

委

員

余仁明

路正偉

中華民國 102 年 7 月 10 日

摘要

Randall-Sundrum 模型提供一個合理的方式解釋新物理和 Higgs Boson 重量的超大修正，並且預測了一個最輕自旋數為 $3/2$ 的 Kaluza-Klein 粒子。我們利用 LHC 的能量尺度找尋經由 pair-production 產生的帶有自旋 $3/2$ 的右旋頂夸克。本篇論文在 19.6 fb^{-1} 的質子質子對撞數據且總碰撞能量為 8 TeV 下，利用 χ^2 sorting 的方法重建 t^* 粒子，此方法包含了找 mass resolution 的值和 neutrino 在 z 方向動量正確率最高的解。我們可以利用 χ^2 和 Likelihood fitter 去估計 data 裡那些從標準模型來的主要背景干擾數量。我們利用質心能量在 7 TeV 且數量為 2.4 到 35.9 pb^{-1} 的單光子數據，來測試這兩種估計方法的正確性。

Abstract

Randall-Sundrum model provides a reasonable way to explain the hierarchy problem and it predicts the lightest spin-3/2 Kaluza-Klein particle. We are searching for the singlet top of spin-3/2 through pair-production that may be produced at LHC energies. This thesis presents the χ^2 sorting method, which includes studies of mass resolution and the probability of getting correct solution of neutrino p_z to reconstruct spin-3/2 particle at $\sqrt{s} = 8$ TeV using 19.6 fb^{-1} of proton-proton collision data collected by CMS. In order to estimate dominated background in data, we also provide two methods, χ^2 fitter and Likelihood fitter. These methods use inclusive photon at $\sqrt{s} = 7$ TeV and the data sample corresponds from 2.4 to 35.9 pb^{-1} .

誌謝

首先感謝我的指導教授余欣珊老師，跟著老師的引領使我這些年受益匪淺，老師的教學熱誠與生活經驗分享也是我最佳典範。論文能夠順利完成，亦是要感謝老師的大力協助。這幾年在學術路上也承蒙許多師長的照顧與提攜，特別感謝張元翰老師、蔣正偉老師、郭家銘老師的幫助，除了課業也讓我們在實驗室享有豐富的資源。

感謝助理張惠虹、曾子庭，以及實驗室學長姐，昀儒、冠昕、佳豫、喬穎、博士後 Marco 以及每個學弟妹們的照顧與陪伴，你們讓我的研究生生活多采多姿，也讓我在高能實驗室裡快快樂樂地度過這幾年的學術歲月。同時也感謝你們不厭其煩的教導我研究中的缺失、為我解惑，你們的幫忙我銘感在心。我的男朋友少甫當然也不能忘記，感謝你的體諒包容，感謝你讓我研究生活充滿樂趣，有你的陪伴總是充滿著笑聲、一掃所有的苦悶。

最後要感謝我的家人，感謝你們全力的支持以及對我無私的付出，使我免於很多煩惱，因為有你們的支持及鼓勵，才有今天的成果，感謝你們。

Content

摘要.....	I
Abstract.....	II
誌謝.....	III

Chapter 1 Introduction 1

1.1 The Standard Model	1
1.2 Search of Heavy Quark t^*	3
1.2.1 The Randall-Sundrum Model	3
1.2.2 Basics of Kaluza-Klein theory	5
1.2.3 Spin-3/2 excitations in the R-S Model.....	7

Chapter 2 CMS Detector in LHC 11

2.1 The Large Hadron Collider	11
2.2 The Compact Muon Solenoid Detector.....	12
2.2.1 Tracker.....	15
2.2.2 Electromagnetic Calorimeter	17
2.2.3 Hadronic Calorimeter	18
2.2.4 Muon Chamber.....	19
2.2.5 Magnet system	20

Chapter 3 Reconstruction of Physics Objects 21

3.1 Software Setup	21
3.1.1 Event Generator	21
3.1.2 Detector Simulation.....	22
3.1.3 Trigger Simulation.....	22
3.2 Final-State Objects Reconstruction.....	22
3.3 Photon Reconstruction.....	24

3.3.1 Photon Selection Variables	24
3.3.2 Track Finding for Conversion	26
3.4 Electron Reconstruction	27
3.4.1 Electron Selection Variables	28
3.4.2 Photon Conversion Rejection	29
3.5 Muon Reconstruction	30
3.6 Jet Reconstruction	30
Chapter 4 Analysis	32
4.1 Monte Carlo Simulation of Background	32
4.1.1 Estimation of Inclusive Photon	34
4.1.2 Photon Purity	39
4.2 Mass χ^2 Sorting	43
4.2.1 Longitudinal Momentum of the Neutrino	43
4.2.2 Mass Resolution	45
Chapter 5 Conclusion	50
Appendix	51
Efficiency	51
Mass Resolution	52
Reference	57

List of Tables

Table 1.1 The fundamental particles of the standard model.....	1
Table 1.2 Examples of baryons.....	2
Table 1.3 Examples of mesons	2
Table 1.4 The four forces that categorize the interactions of the particles	3

Table 2.1 The principal characteristics of the CMS solenoid magnet.....	20
Table 4.1 List of processes and cross sections used for the normalization of the Monte Carlo samples.....	32
Table 4.2 List of processes and cross sections used for the normalization of the Monte Carlo samples.....	33
 A-1 Signal efficiency with a function of pt.....	51
A-2 Signal efficiency with a function of eta.....	51
A-3 Hadronic W Mass Resolution	52
A-4 Hadronic top Mass Resolution	53
A-5 Hadronic t^* Mass Resolution.....	54
A-6 Leptonic top Mass Resolution	55
A-7 Leptonic t^* Mass Resolution	56

List of Figures

Figure 1.1 RS model	4
Figure 1.2 The 5th space is compactified.....	4
Figure 1.3 To define parity in a circle.....	5
Figure 1.4 Mass gap of KK tower $\Delta m \sim 1/R$	7
Figure 1.5 The ground state and the excited state.	7
Figure 1.6 The mass of the fist KK mode of a spin-3/2 resonance as a function of the bulk mass parameter c	8
Figure 1.7 The mass of the first KK mode of spin-3/2 quark excitations as a function of the string bulk mass parameter s	9
Figure 1.8 Feynman diagrams contributing to pair-production of singlet top spin-3/2 resonances (double lines).	10
Figure 2.1 CERN Accelerator Complex.	11
Figure 2.2 View of the LHC location.....	12
Figure 2.3 The CMS detector overview.....	13
Figure 2.4 The CMS coordinate system.....	14
Figure 2.5 Pixel detector in the CMS Tracker.....	15
Figure 2.6.....	16
Figure 2.7.....	16
Figure 2.8 Layout of one quarter of CMS ECAL.....	17

Figure 2.9 Longitudinal view of one quadrant of CMS	18	
Figure 2.10 the position of the three different chamber designs.....	19	
Figure 3.1 Overview of analysis flow in the CMSSW.....	21	
Figure 3.2 Hybrid Supercluster Algorithm.....	23	
Figure 3.3 Multi 5 \times 5 Algorithm	23	
Figure 3.4 Sketch of Photon Isolation to study of what else is in the detector.	26	
Figure 3.5 Sketch of inward-outward track	27	
Figure 3.6 GSF used for Bremsstrahlung emission in the tracker	28	
Figure 3.7 MissingHits.	29	
Figure 3.8 Muon reconstruction.	30	
Figure 3.9 Collinear safety	Figure 3.10 Infrared safety	31
Figure 3.11 Colored areas represent anti-kt clustered jets.....	31	
Figure 4.1 Distribution of the reconstructed invariant mass.	34	
Figure 4.2 Feynman diagram of the leading order photon process	35	
Figure 4.3 Transverse shower shapes with crystals..	35	
Figure 4.4 Several χ^2 probability distributions for different degree of freedom.....	36	
Figure 4.5 Sigma of the pull distributions in pseudo-experiments.....	40	
Figure 4.6 Average of the pull distributions in pseudo-experiments.....	40	
Figure 4.7 Fitting shower shape ($\sigma_{inj\eta}$) variable with 12 Pt bins in Barrel region.....	41	
Figure 4.8: Fitting shower shape ($\sigma_{inj\eta}$) variable with 12 Pt bins in Barrel region....	42	
Figure 4.9 The various abs(NuPz - XXX).	44	
Figure 4.10 Mass resolutions.	45	
Figure 4.11 Hadronic W's mass resolution as a function of signal mass.	46	
Figure 4.12 Hadronic top's mass resolution as a function of signal mass.	47	
Figure 4.13 Hadronic t^* mass resolution as a function of signal mass.....	47	
Figure 4.14 Leptonic top mass resolution as a function of signal mass.	48	
Figure 4.15 Leptonic t^* mass resolution as a function of signal mass.....	48	
Figure 4.16 Leptonic t^* mass resolution as a function of signal mass.....	49	

Chapter 1 Introduction

The thesis is structured as follows. The first chapter introduces the Standard Model (SM) and explains which model predict spin-3/2 particle that can be produced at LHC energy. Then the experimental setup will be given, focusing on the LHC accelerator and the CMS detector. The discussion of the reconstruction of the particle objects is in Chapter 3. After that, it is described the event background and the method to estimate background. In the subsequent section, the selection of longitudinal momentum of the neutrino and the mass resolution of the χ^2 sorting method are discussed. The conclusion will be given in Chapter 5.

1.1 The Standard Model

In the standard model (SM Table 1.1), the matter is made out of two categories, fermions and bosons. There are twelve known fermions, six quarks and six leptons, falling into three generations. The six leptons are classified according to their charge, electron number, muon number and tau number. Similarly, there are six “flavors” of quarks (up, down, charm, strange, top, bottom). For each particle, there is an anti-particle with opposite charge.

Table 1.1 The fundamental particles of the standard model. [1]

FERMIONS		
Leptons spin = 1/2		
Flavor	Mass GeV/c ²	Electric charge
ν_L lightest neutrino*	$(0-0.13) \times 10^{-9}$	0
e electron	0.000511	-1
ν_M middle neutrino*	$(0.009-0.13) \times 10^{-9}$	0
μ muon	0.106	-1
ν_H heaviest neutrino*	$(0.04-0.14) \times 10^{-9}$	0
τ tau	1.777	-1
Quarks spin = 1/2		
Flavor	Approx. Mass GeV/c ²	Electric charge
u up	0.002	2/3
d down	0.005	-1/3
c charm	1.3	2/3
s strange	0.1	-1/3
t top	173	2/3
b bottom	4.2	-1/3

The only colorless hadrons we can make are $q\bar{q}$ (the mesons), qqq (the baryons), and $\bar{q}\bar{q}\bar{q}$ (the antibaryons). Some of the baryons and mesons are shown

in Table 1.2 and Table 1.3 separately.

There are four forces in nature; all of them can correspond to four interactions, strong, electromagnetic, weak, and gravitational force. Both quarks and leptons are spin-1/2 particles that can participate in weak interactions. Not all particles participate in strong interactions like leptons. And neutrinos are electrically neutral; they are not affected by the electromagnetic interactions. The charged W and neutral Z bosons are the mediators for the weak interactions. Electromagnetic interactions are mediated by photon and photon couples to electric charge with interaction strength proportional to that charge. In addition to the electric charge, color charge is a property of quarks and gluons that is related to the strong interactions of the particles. The strong force confines quarks inside protons and neutrons and it increases its strength when the increased distance of two quarks. The gravity is expected to be mediated by the exchange of the graviton but it has not been discovered by experiments. Each force is shown in Table 1.4.

Table 1.2 Examples of baryons. [1]

Baryons qqq and Antibaryons $\bar{q}\bar{q}\bar{q}$					
Baryons are fermionic hadrons.					
These are a few of the many types of baryons.					
Symbol	Name	Quark content	Electric charge	Mass GeV/c^2	Spin
p	proton	uud	1	0.938	1/2
\bar{p}	antiproton	$\bar{u}\bar{u}\bar{d}$	-1	0.938	1/2
n	neutron	udd	0	0.940	1/2
Λ	lambda	uds	0	1.116	1/2
Ω^-	omega	sss	-1	1.672	3/2

Table 1.3 Examples of mesons. [1]

Mesons $q\bar{q}$					
Mesons are bosonic hadrons					
These are a few of the many types of mesons.					
Symbol	Name	Quark content	Electric charge	Mass GeV/c^2	Spin
π^+	pion	u\bar{d}	+1	0.140	0
K^-	kaon	s\bar{u}	-1	0.494	0
ρ^+	rho	u\bar{d}	+1	0.776	1
B^0	B-zero	d\bar{b}	0	5.279	0
η_c	eta-c	c\bar{c}	0	2.980	0

Table 1.4 The four forces that categorize the interactions of the particles. [1]

BOSONS		
Unified Electroweak spin = 1		
Name	Mass GeV/c ²	Electric charge
γ photon	0	0
W^-	80.39	-1
W^+	80.39	+1
W bosons		
Z^0 Z boson	91.188	0

Strong (color) spin =1		
Name	Mass GeV/c ²	Electric charge
g gluon	0	0

1.2 Search of Heavy Quark t^*

The LHC is designed not only to confirm the predictions of the SM, but also to discover new physics models including exotic fermions not present in the SM. Among exotic fermions one possible new particle is a spin-3/2 excitation of quarks. A heavy spin-3/2 quark could also exist as lighter than the Kaluza-Klein (KK) excitation modes [2] in string theory if it is compactification [3] (see Section 1.2.1). Randall-Sundrum (RS) [4] model can explain the hierarchy between the weak scale and the Planck scale and it predicts that heavy KK particles may be produced at LHC energy. The introduction of RS model including the bulk geometry and the meaning of compactification will be described first. The KK excitation mode is given in Section 1.2.2. Finally, the production of the spin-3/2 excitation is described in Section 1.2.3.

1.2.1 The Randall-Sundrum Model

The model presented by Lisa Randall and Raman Sundrum in 1999 which provides a new explanation of problem of the hierarchy between the electroweak and Planck scales (see Figure 1.1). In the original RS model only gravity propagates in the bulk, but it was soon believed that the Standard Model fields can live in the warped extra dimension to solve the issue like the hierarchy of fermion masses [5]. The bulk geometry will be presented in this section and the meaning of the compactification is narrated in the last part of this section.

Island Universes in Warped Space-Time

According to string theory, our universe might consist of a three-dimensional “brane,” embedded in higher dimensions. In the model developed by Lisa Randall and Raman Sundrum, gravity is much weaker on our brane than on another brane, separated from us by a fifth dimension. (Time is the unseen fourth dimension.)

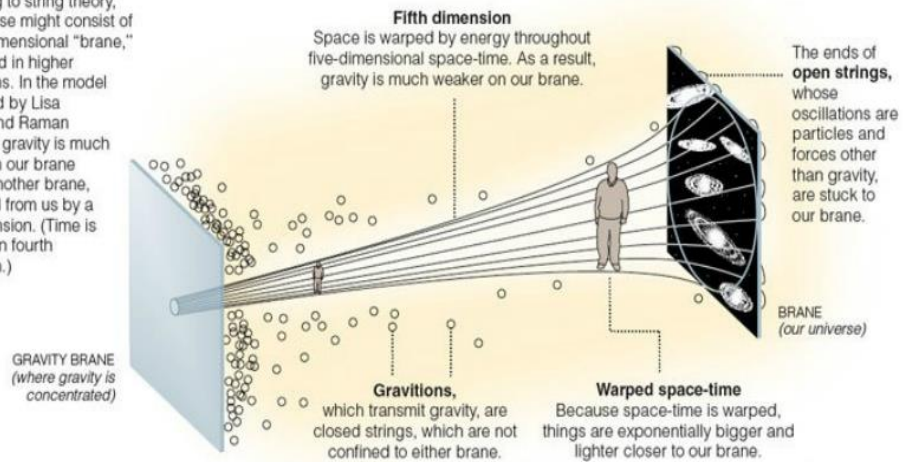


Figure 1.1 The RS model is a 5-dimensional spacetime with a warped geometry. [6]

The throat (extra dimension) [7] in the RS model is bound by two branes, the ultra-violet brane (UV) at $y = \pi R$ and the infra-red (IR) brane at $y = 0$ (see Figure 1.2). The throat forms thick slices so it often called bulks. The Planck brane is a five dimensional space and it is curled to a small size (Planck scale). Each of slice is a four dimensional space. The slices which are close to UV brane are the Planck scale and the slices which are close to IR brane are in the TeV scale.

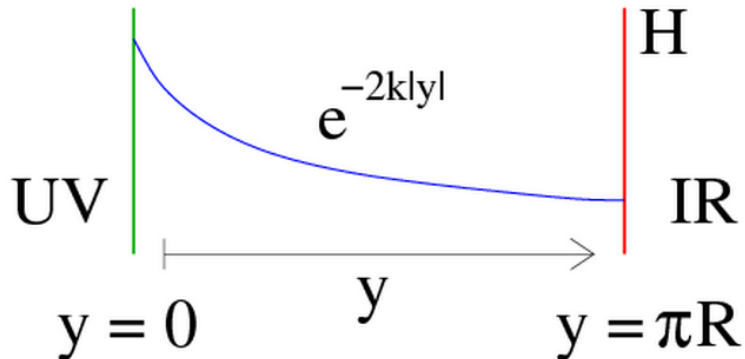


Figure 1.2 The 5th space is compactified. Brane at $y=0$ is called UV or Planck Brane.

Brane at $y=L$ is called IR or TeV Brane. [8]

Orbifold Compactification

An orbifold (orbit-manifold) can help us to define “parity” in a circle. Let us consider one extra dimension which is the compact space S^1/\mathbb{Z}_2 , where S^1 is the circle group and \mathbb{Z}_2 is the group that identify points opposite in the circle ($\phi \rightarrow -\phi$).

It means the extra dimension has the properties of periodicity ($y \rightarrow y + \pi R$) and orbifold symmetry $[(x^\mu, \phi) = (x^\mu, -\phi)]$, see Figure 1.3, where ϕ is the angular coordinate for the fifth dimension].

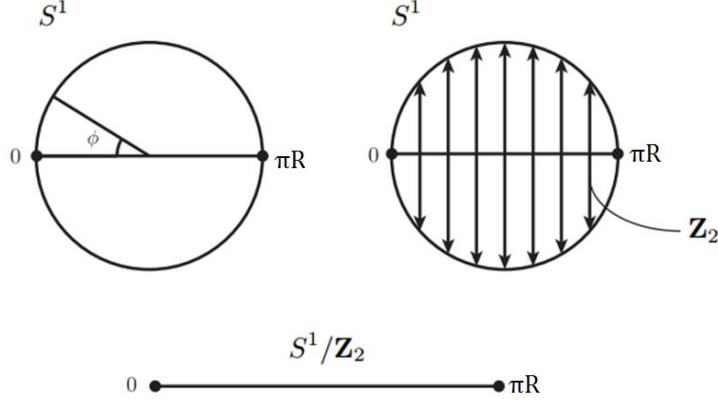


Figure 1.3 To define parity in a circle. [9]

Thus circle reduced to segment with fixed points at 0 and πR by the \mathbf{Z}_2 group. The fields can be even or odd under $\phi \rightarrow -\phi$ in extra dimension, so bulk fermions have chiral zero modes (Left-Handed or Right-Handed).

Warped Metric

It is the model with the exponential warping of the bulk geometry. The energy scale at one end of the extra dimension is much larger than at the other end due to the warp factor which generates a large ratio of energy scales.

$$ds^2 = e^{-2k(y)} \eta_{\mu\nu} dx^\mu dx^\nu + dy^2,$$

where $\eta_{\mu\nu} = \text{diag}(-1, 1, 1, 1)$ is the four-dimensional Minkowski metric, $e^{-2k(y)}$ is the warp factor which causes the special geometry of the space and k is AdS curvature. The warp factor allows solving the gauge hierarchy problem if the Higgs field is located at the IR brane.

1.2.2 Basics of Kaluza-Klein theory

In order to unify Electromagnetic and gravitational fields, Kaluza and Oskar Klein developed this method in the middle of the 1920's. His basic idea was to consider the case of an extra dimension, the fifth dimension. In 1926 Oskar Klein assumed the extra

dimension to be compact. It means the space obtained is the four-dimensional Minkowski space with a circle, $\mathbf{R}^4 \times \mathbf{S}^1$, and the fifth coordinate is periodic, $0 \leq y \leq 2\pi R$, where R is the radius of the circle. The Kaluza-Klein modes can be produced by this fifth dimension. If spatial dimension is compact then momentum in that periodic dimension is quantized:

$$p^5 = \frac{n}{R}$$

Where $n \in \mathbb{Z}$. Let us first define our notation: hatted quantities will be the five-dimensional ($\hat{\mu}$) and unhatted one will be the four-dimensional field (μ). Five-dimensional indices are denoted $\hat{\mu} = 0, 1, 2, 3, 5$ and the four-dimensional indices are denoted $\mu = 0, 1, 2, 3$ [$x^{\hat{\mu}} = (x^\mu, y)$]. Then we expand the massless scalar field $\phi(x^\mu, y)$ in Fourier series:

$$\phi(x^\mu, y) = \sum_{n=-\infty}^{n=\infty} \phi^n e^{iny/R}$$

We put this scalar field with a quantized momentum ($\frac{n}{R}$) into equation of motions

$(\partial_\mu \phi \partial^\mu \phi - \partial_s \phi \partial^s \phi)$, it becomes:

$$\sum_n [\partial_\mu \phi_n(x) \partial^\mu \phi_n(x) - \frac{n^2}{R^2} \phi_n \phi_n]$$

In this way, the tower of fields with masses $m^2 = \frac{n^2}{R^2}$ is generated. This infinite tower of fields is called Kaluza-Klein states and they are generated in the direction of extra dimensions. Each mass gap of KK states is about $1/R$ (Fig. 1.4) and the KK mass n/R is about TeV scale. It implies a radius constraint:

$$R < 10^{-21} \text{ cm.}$$

An experimental bound on the size of the compactification radius R in such minuscule dimensions points out the fact that those KK particles are hard to seek at LHC.

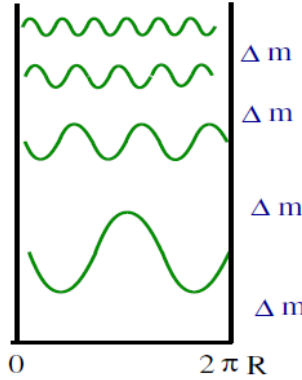


Figure 1.4 Mass gap of KK tower $\Delta m \sim 1/R$

1.2.3 Spin-3/2 excitations in the R-S Model

As for the case of the massless scalar fields (see Section 1.2.2), the spin-3/2 field admits to be the form:

$$\Psi_\mu^{L,R}(x, y) = \frac{1}{\sqrt{L}} \sum_n \psi_{\mu n}^{L,R}(x) e^{2ky} f_n^{L,R}(y)$$

With the 4D chiral components $\psi_{\mu n}^{L,R}$, the KK mode-function are normalized as:

$$\frac{1}{L} \int_0^L dy e^{ky} f_m^{L,R*} f_n^{L,R} = \delta_{mn}.$$

To calculate the spectrum of the excited states from five-dimension, we can think of it as potential well. KK modes are like the solutions of potential well (See the Figure 1.5).

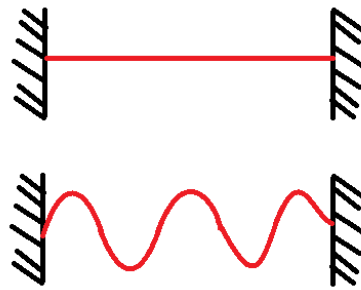


Figure 1.5 The upper figure is the ground state and the lower one is the excited state.

Therefore we put the spin-3/2 fields into equations of motion and derive:

$$(\partial_5 + M_\Psi) f_n^R = m_n e^{ky} f_n^L, \\ (-\partial_5 + M_\Psi) f_n^L = m_n e^{ky} f_n^R,$$

where m_n is the 4D (Dirac) mass of the n -th KK mode. To determine the KK spectrum, we impose the distinct boundary conditions (b.c.), $(-,+)$ and $(+,-)$ for the mode functions. Where $-$ refers to Dirichlet and $+$ to Neumann, in the (UV, IR) branes. In the limit that Dirichlet-Neumann (Neumann-Dirichlet), the fields will be forced to vanish on the IR (UV) brane (because there is no spin-3/2 SM elementary particle). These equations have the general solution:

$$f_n^R(t) = \sqrt{t} \left[a_n^R J_{c+\frac{1}{2}}(x_n t) + b_n^R J_{-c-\frac{1}{2}}(x_n t) \right], \\ f_n^L(t) = \sqrt{t} \left[a_n^L J_{\frac{1}{2}-c}(x_n t) + b_n^L J_{c-\frac{1}{2}}(x_n t) \right],$$

where $J(x)$ represents a Bessel function. It is worth noting that the wave function is also fixed by the bulk mass parameter c_0 . The following discussions will describe the bulk mass parameters more.

Bulk Fermion Masses

The bulk mass of the spin-3/2 resonances include the mass of its spin-1/2 SM fermion, c_{0i} , and an extra string contribution, s . Therefor the bulk mass for resonance i : $c_i = c_{0i} + s$ where the value of s could be larger than zero or smaller than zero. The redefinition bulk mass parameter, $c \rightarrow -c$, that symmetrically describes the mass of the first KK mode in different boundary condition, see Fig. 1.6. It shows that there exist values of c for which this mode can become quite light.

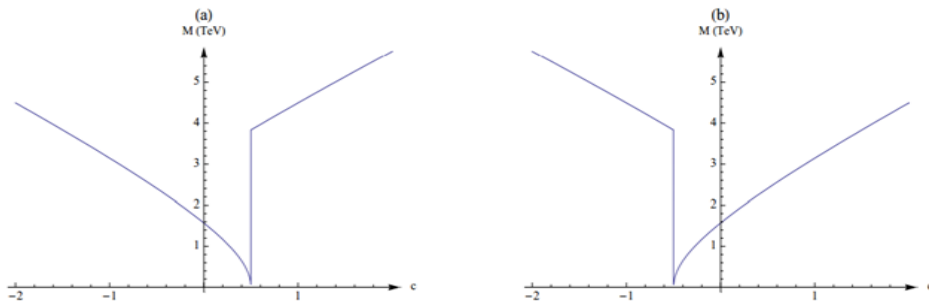


Figure 1.6 It is the mass of the fist KK mode of a spin-3/2 resonance as a function of the bulk mass parameter c . [10] The left hand side is the b.c $(-,+)$ and the right hand side is the b.c $(+,-)$.

Parameter c_0

The more realistic and theoretically satisfying model would be all SM fermions and gauge bosons living in the extra dimension; but the Higgs boson is confined to the IR (or TeV) brane in order to generate spontaneous symmetry breaking. Through spontaneous symmetry breaking [11, [12], the fermions obtained their mass by Yukawa coupling to a scalar vacuum expectation value of the Higgs field. The 5-dimensional Yukawa coupling strength are given by

$$\lambda_{u,d} = \lambda_5 k \left(\frac{\frac{1}{2} + c_{0u,d}}{e^{(1+2c_{0u,d})kL} - 1} \right)^{\frac{1}{2}} \left(\frac{\frac{1}{2} + c_{0q}}{e^{(1+2c_{0q})kL} - 1} \right)^{\frac{1}{2}} e^{(1+c_{0u,d}+c_{0q})kL},$$

where k is the KK scale. This indicates that the wave function near the UV brane with small Yukawa couplings when $c_0 \leq -1/2$ and near the UV brane with large Yukawa couplings when $c_0 > 1/2$.

Because the problem of flavor mixing, we try to fit bulk mass and find out the allowable parameter: only 3^{rd} generation can localize on IR brane. We further confine that only right hand top which is $c_0 > 1/2$ can localize on IR brane. Therefore it is very different between singlet top and others fermions.

Parameter s

Mass spectrum of spin-3/2 quark excitations (first KK mode) is shown in Fig.1.7.

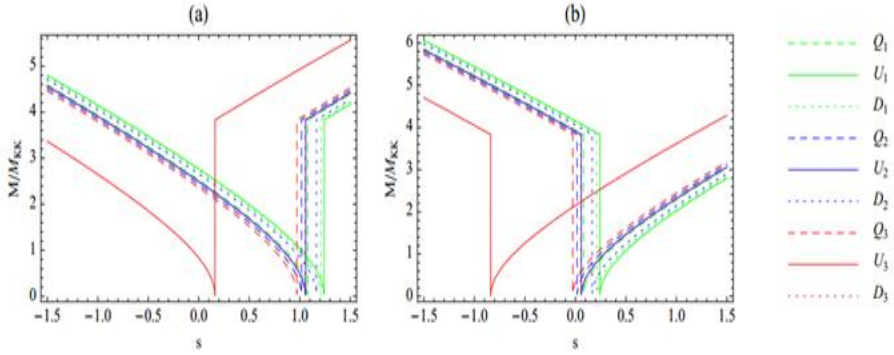


Figure 1.7 It is the mass of the first KK mode of spin-3/2 quark excitations as a function of the string bulk mass parameter s . Masses are normalized to the nominal KK scale. [10] The left hand side is the b.c. $(-,+)$ and the right hand side is the b.c. $(+,-)$. Recall that the bulk mass is $c_i = c_{0i} + s$. We suppose all spin-3/2 particles have the same s value because parameter s is not the flavor contribution. In $s < 0$ case, the

mass of right-handed t^* ($c_0 > 1/2$) is smaller than the mass of others particles ($c_0 \leq -1/2$):

$$t^* \text{ mass} = \left| \frac{1}{2} - s \right| < \text{others mass} = \left| -\frac{1}{2} - s \right|$$

The fig.1.9 clearly shows that the singlet top excitation is lighter (heavier) than all other for negative (positive) s and it may even lie below the KK scale. Therefore the right-handed top spin-3/2 resonance is lighter than all others in a large region of parameter space.

We search the decay mode of t^* to be into a top and photon and consider the pair-production because the cross-section of pair-production at the LHC is larger than single-production. Fig. 1.8 shows the Feynman diagrams of pair-production which include gluon-fusion and quark-antiquark annihilation.

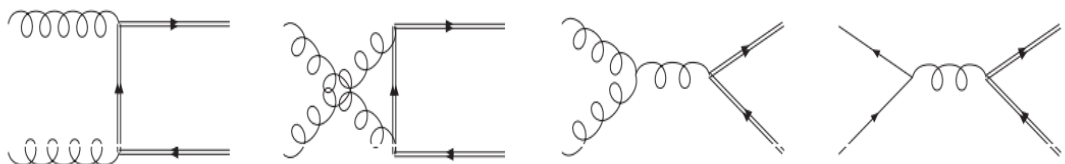


Figure 1.8 Feynman diagrams contributing to pair-production of singlet top spin-3/2 resonances (double lines). [10]

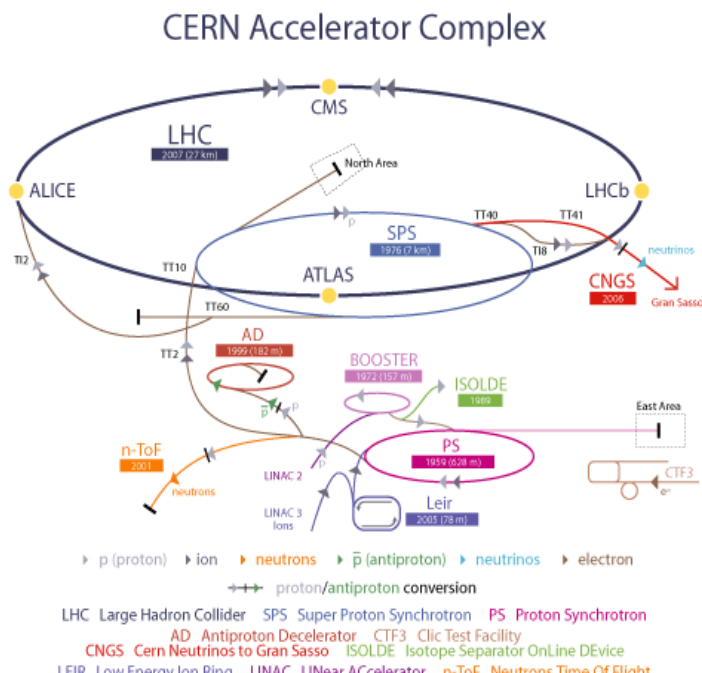
Chapter 2 CMS Detector in LHC

The Large Hadron Collider (LHC) was built by the European Organization for Nuclear Research (CERN), and the 27-kilometre LHC is the world's largest and highest-energy particle accelerator. In the LHC, particle beams are accelerated up to the record energy of 4 TeV per beam allowing the experiment to reproduce the similar state after the Big Bang.

2.1 The Large Hadron Collider

Before being transferred to the main LHC ring, the particle beams go through a succession of machines that accelerate them to higher energies (Fig2.1). The beam source is a simple bottle of hydrogen gas, and an electric field is used to strip hydrogen atoms to yield protons. Linac 2, the first linear accelerator can accelerate the beam up to 50 MeV. The proton beam is then injected into the Proton Synchrotron Booster (PSB) and accelerated to 1.4 GeV. Proton Synchrotron (PS), the following machine pushes the beam to 25 GeV and then the protons are sent to the Super Proton Synchrotron (SPS) where the beams is up to 450 GeV. Finally in the last element of chain, Large Hadron Collider (LHC), it is accelerated energy up to 4 TeV per beam. Two high-energy particle beams travel at the speed of 0.99999991C.

Fig. 2.1 CERN Accelerator Complex. [13]



LHC ring accelerates two beams of protons in opposite directions and each beam consists of a large number of bunches of protons which would help them to be accelerated and also to ensure greater numbers of collisions. Furthermore the superconducting magnets at liquid helium temperature help two beams of protons to focus in a circular path. The beam is accelerated by cavities of electric field. There are eight places around the ring where the beam is accelerated and four detectors where the two beams are brought into collision, A Large Ion Collider Experiment (ALICE), A Toroidal LHC Apparatus (ATLAS), Compact Muon Solenoid (CMS) and the Large Hadron Collider Beauty Experiment (LHCb), (Figure 2.2).

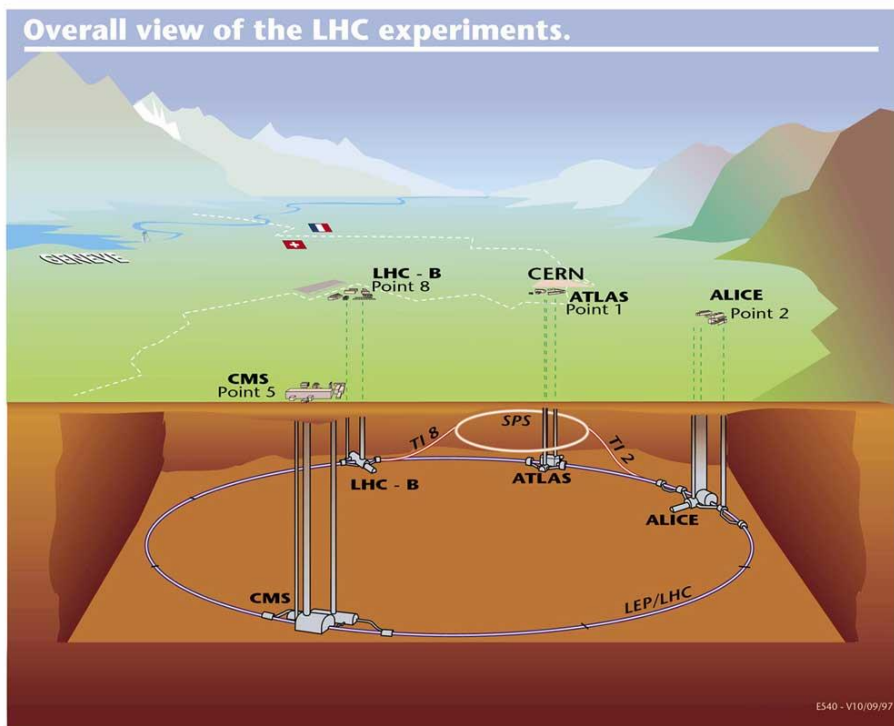


Figure 2.2 View of the LHC location.

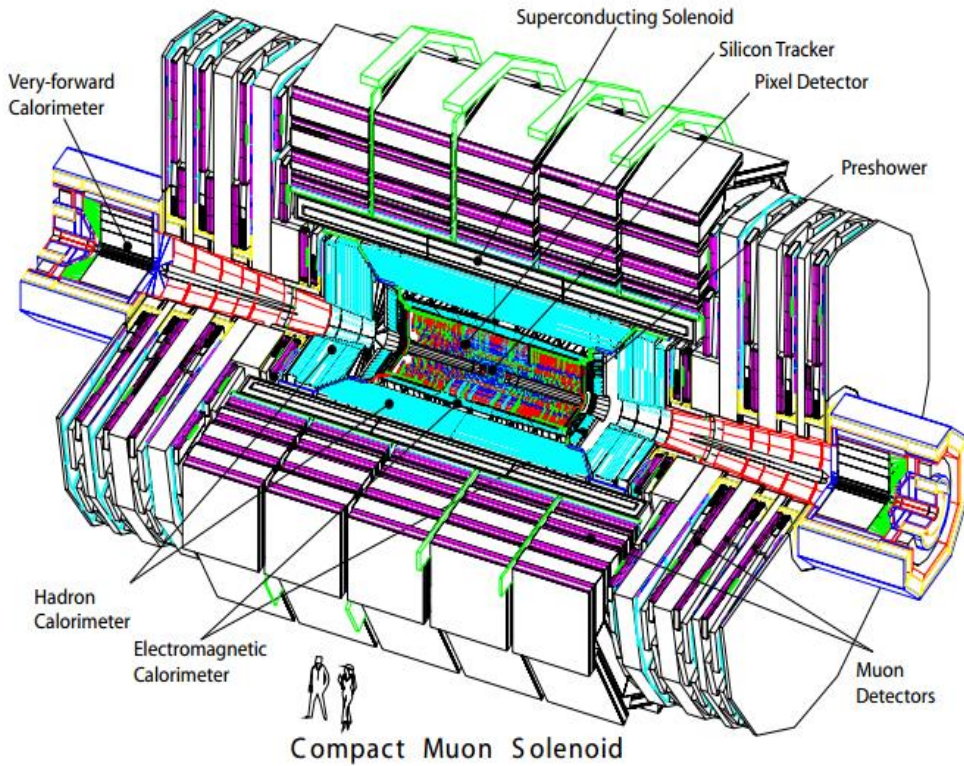
2.2 The Compact Muon Solenoid Detector

The goals of the Compact Muon Solenoid (CMS) [14] are to explore physics at the TeV scale, to discover the Higgs boson and to find the physics beyond the standard model like extra dimensions. CMS and ATLAS use different magnet-system design and technical solutions to achieve the goals.

Now it's about CMS. The complete detector forms a cylindrical coil of superconducting cable that generates about 3.8-tesla magnetic field with 21.6 m long, 15 m diameter and about 12500-tonne weight and it is located 100 m underground near Cessy in France.

The design configuration is shown in Figure 2.3. It contains subsystems, the inner tracker and the calorimeters; they are essential to measure collision particle's

Figure 2.3 The CMS detector overview. [15]



momentum from leaving cured tracks in the magnetic field and energy from calorimeters. The innermost layer is tracker with 3 layers of silicon pixel detectors in order to improve the momenta measurement of the charge-particles. Surrounding the tracker is the EM calorimeter (ECAL) that uses lead tungstate (PbWO_4) and measures the energy of electrons and photons. In the EndCap regions, a preshower system sits in front of the ECAL to prevent such as π_0 false signals. Then the Hadronic Calorimeter (HCAL) measures the energy of hadron particles which is made of quarks and gluons. It has coverage up to $|\eta| < 3.0$. The outside layouts are the superconducting solenoid magnet and four muon stations, which are interleaved with iron "return yoke" plates.

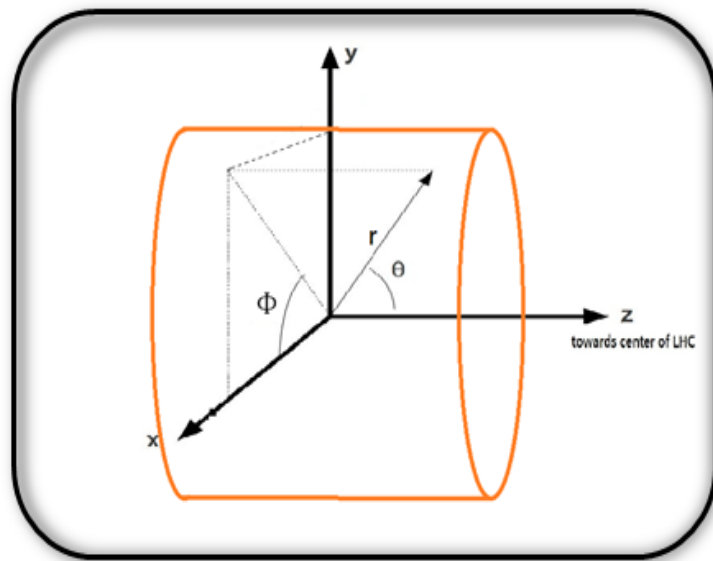
The CMS coordinate system (Figure 2.4) is defined such that the z-axis coincides with the direction along the proton beam line. The horizontal x-axis points radially towards the accelerator ring center. And hence the y-axis is vertical and points up. The notation r is the distance from the z-axis and the polar angle θ is the measurement angle from the positive z-axis. $\theta = 0$ is positive axis and $\theta = \pi$ is negative z axis. The azimuthal angle (ϕ) is the evaluated from the plane that is

perpendicular z-axis, $\phi = 0$ is positive x axis and $\phi = \frac{\pi}{2}$ is positive y axis.

A useful kinematic variable for hadron collider is the function of the pseudo rapidity that is defined by the polar angle,

$$\eta = -\ln(\tan(\frac{\theta}{2})).$$

Fig 2.4 The CMS coordinate system



The pseudorapidity is convenient. The distribution would only lead to a shift when changing coordinate system. The pseudorapidity is also used to define the barrel, endcap, and forward regions of the CMS detector. An angular distance ΔR is defined as a combination of distances in ϕ and η ,

$$\Delta R = \sqrt{(\Delta\phi)^2 + (\Delta\eta)^2}.$$

The transvers energy E_T and the momentum P_T are the boost invariant,

$$E_T = E \cdot \sin \theta \text{ and } P_T = P \cdot \sin \theta.$$

2.2.1 Tracker

The most inner part of the CMS detector is the silicon tracker [16, [17]. The layout of CMS Tracker is shown in Figure 2.5.

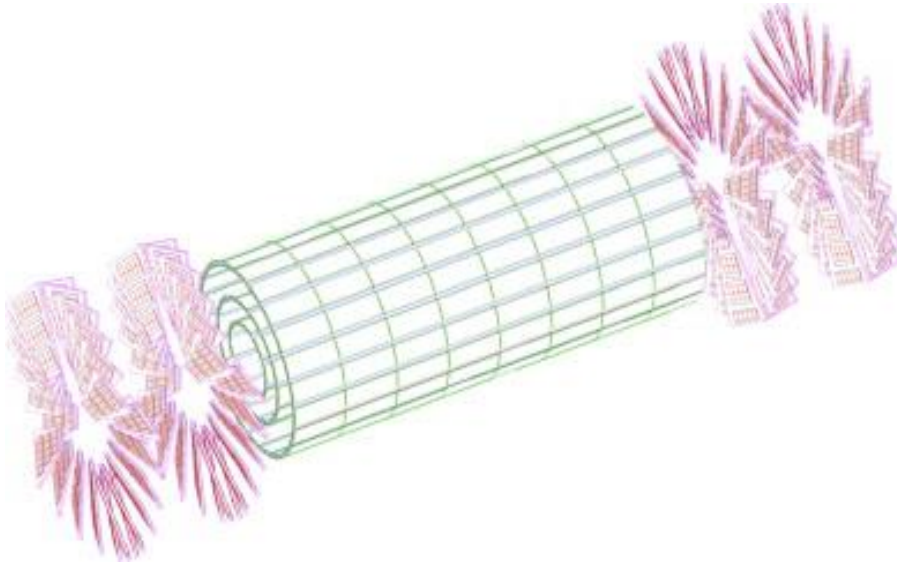


Figure 2.5 Pixel detector in the CMS Tracker. [15]

The one purpose is to measure the curvature of trajectories then to derive charged particle's momentum as precisely as possible. The Lorentz Force bends the tracks in the $r\phi$ -plane because of the solenoidal magnetic field.

$$\vec{F}_L = \frac{q}{m} \vec{p} \times \vec{B}.$$

Moreover, minimizing the effects of the material budget of the inner tracking system is required. Trackers will affect photons and electrons before reaching electromagnetic calorimeter. For example, photons produce electron pair when traversing the tracker material. Figure 2.6 shows the fractional radiation length as a function of pseudorapidity. In the barrel region the tracking system consists of the Tracker Inner Barrel (TIB) and Tracker Inner Disks (TID) as endcaps, each composed of three small discs.

The outer Barrel (TOB) with six concentric layers is closed by the Tracker End Caps (TEC) which are the two endcaps detectors on either side of the detector like Figure 2.7 showing. And the pixel detectors is the CMS detector's center interaction

region, it is used to reconstruct the primary and secondary vertices.

Tracker Material Budget

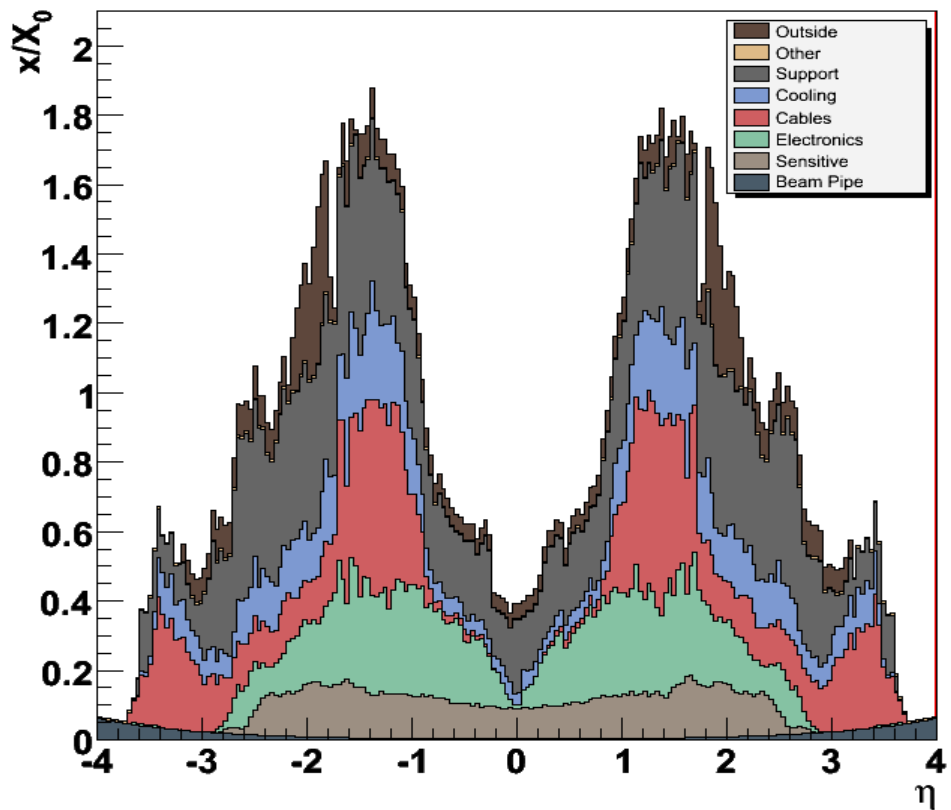


Figure 2.6

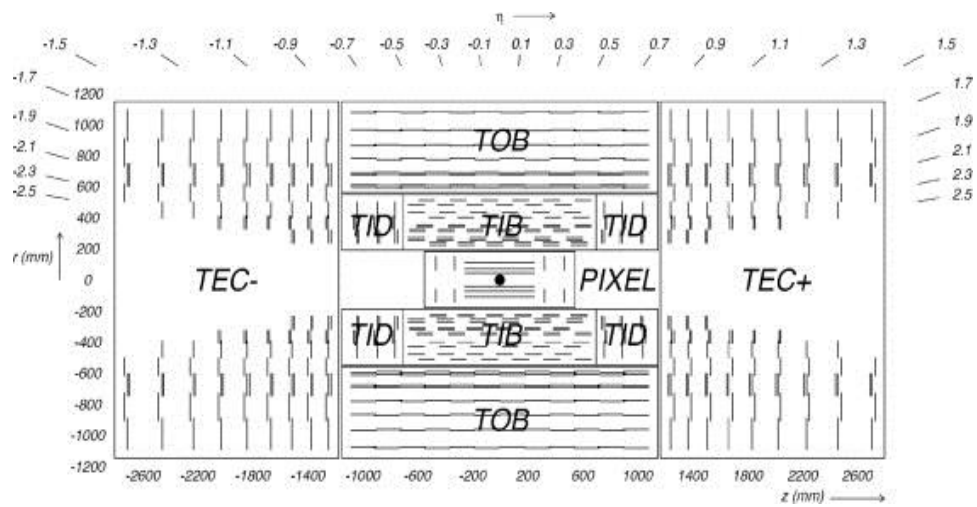


Figure 2.7

For this analysis, tracking system can improve the overall jet energy measurement by matching associated tracks. And it also plays an important role for

finding the leptonically decaying W boson in t^* decay mode. It will be discussed again in Chapter 3. Furthermore it is used to suppress background processes and to find the secondary vertex of particle with short lifetime like B-hadrons.

2.2.2 Electromagnetic Calorimeter

The tracking system is fully enclosed by the Electromagnetic Calorimeter (ECAL) [18, [19]. The ECAL helps to measure photons and electrons energy by fully stopping them. These high energetic particles create electromagnetic showers in material. Then to do Track-Cluster matching can help to select good particle candidates. The ECAL separates into a barrel (EB) which corresponding to the range $|\eta| < 1.479$ and an endcap (EE) which corresponding the range $1.6 < |\eta| < 2.6$. A Preshower detector (ES) followed by a PbWO_4 calorimeter in endcaps region as shown in Figure 2.8.

The ECAL is composed of scintillating lead tungstate crystals (PbWO_4) like above descriptions. There are about 61000 crystals in the EB and about 7300 crystals in the EE. The preshower device is made of silicon strip and it helps to reject electrons and photons from fake signature by the showering process.

The energy resolution of the ECAL can be calculated as follows [20]:

$$\left(\frac{\sigma}{E}\right)^2 \approx \left(\frac{N}{E}\right)^2 + \left(\frac{S}{\sqrt{E}}\right)^2 + C^2$$

The N is the term of electronic noise and event pile-up. The S is the term of the stochastic and C represents the constant term.

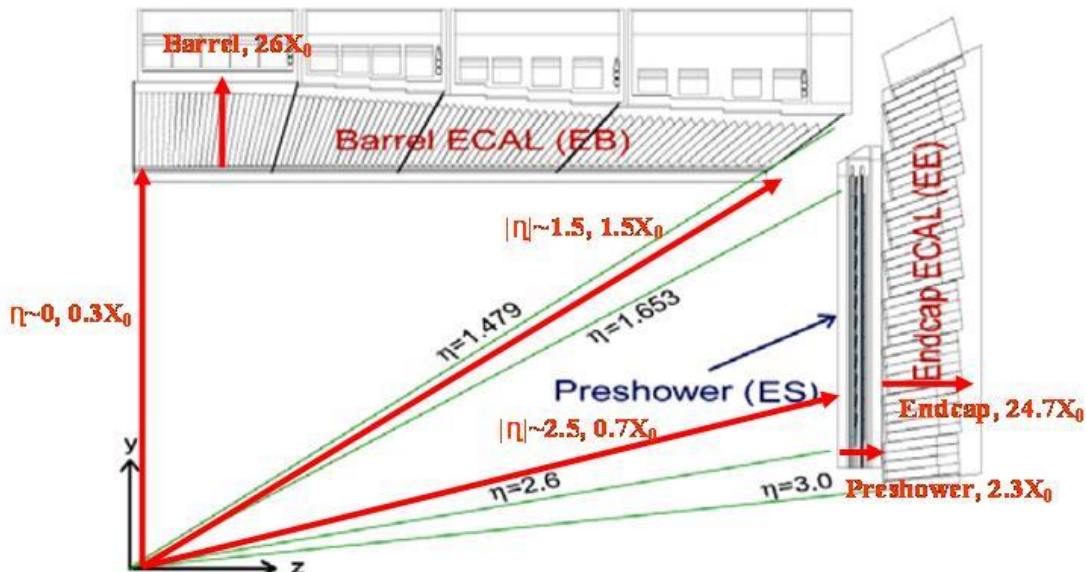


Figure 2.8 Layout of one quarter of CMS ECAL.

Preshower includes $2.3X_0$ of Pb absorber. Each Endcap calorimeter is made about $24.7X_0$ in depth and Barrel is about $26X_0$ in depth.

2.2.3 Hadronic Calorimeter

The hadron calorimeter (HCAL) [21] is used together with ECAL to measure jets energy by full absorption. To measure the final products of hadronisation is done by the combination of the hadronic and the electromagnetic calorimeter. This device is important to the reconstruction of quarks (jets) from the t^* decays. Its absorber material is made from copper alloy and sensitive material is made from plastic scintillator. The structure of the Barrel Hadronic Calorimeter (HB) and the Endcap Hadronic Calorimeter (HE) that both are inside the magnetic coil, the former covers the central pseudorapidity up to about $|\eta| = 1.3$ and the latter extends the angular coverage in $1.3 < |\eta| < 3$ (See Figure 2.9). The Forward Hadronic Calorimeter (HF) located 11 m either side of the interaction point. Its pseudorapidity covers up to $|\eta|=5$. The Out Hadron Calorimeter (HO) or called Tail Catcher rests outside the magnetic coil as well into barrel region.

The energy resolution of HCAL is given by the formula [22],[23]:

$$\left(\frac{\sigma}{E}\right)^2 \approx \left(\frac{0.71}{E}\right)^2 + \left(\frac{0.97}{\sqrt{E}}\right)^2 + 0.08^2$$

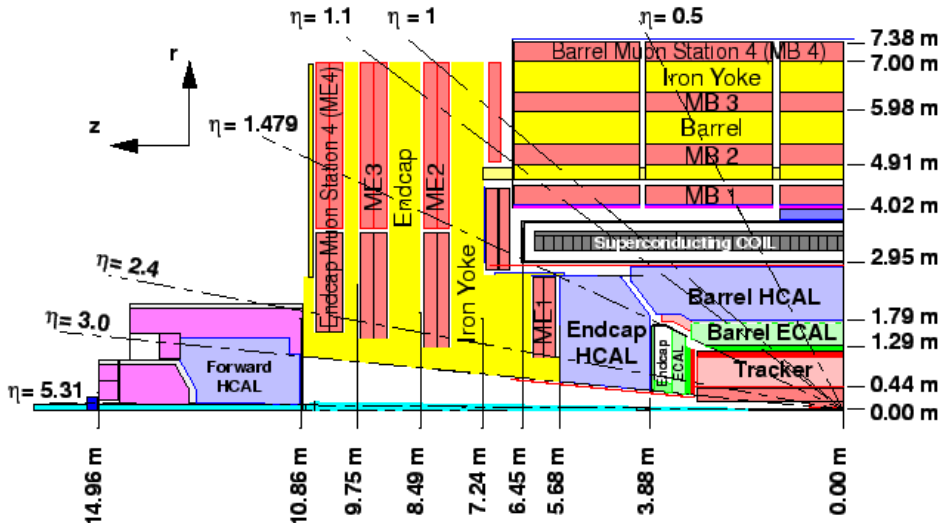


Figure 2.9 Longitudinal view of one quadrant of CMS

2.2.4 Muon Chamber

Because relatively long life time's muons pass without interaction through the detector, so the system is placed the outermost of the detector. The muon chamber [24] are embedded into the return yoke of the superconducting magnet. The muon system enables to good identify and measure of these muons by using three types of detector: Drift Tubes (DT), Cathode Strip Chambers (CSC) and Resistive Plate Chambers (RPC).

The DTs are used to measure position in the barrel region with the $|\eta| < 1.2$ range. The CSCs are chosen for measuring the endcaps region position with coverage up to $|\eta| < 2.4$, where the particle rate is higher. The RPC are fast gaseous detectors which are both in the barrel and in the endcaps. And it also provides accurate time measurements. The schematic layout is shown in Figure 2.10.

The DT and CSC position resolution are better than 100 μm and 200 μm separately. The DT is approximately 1 mrad in ϕ direction and CSC is about 10 mrad. And the time resolution with the combination of good spatial resolution is better than three nanoseconds.

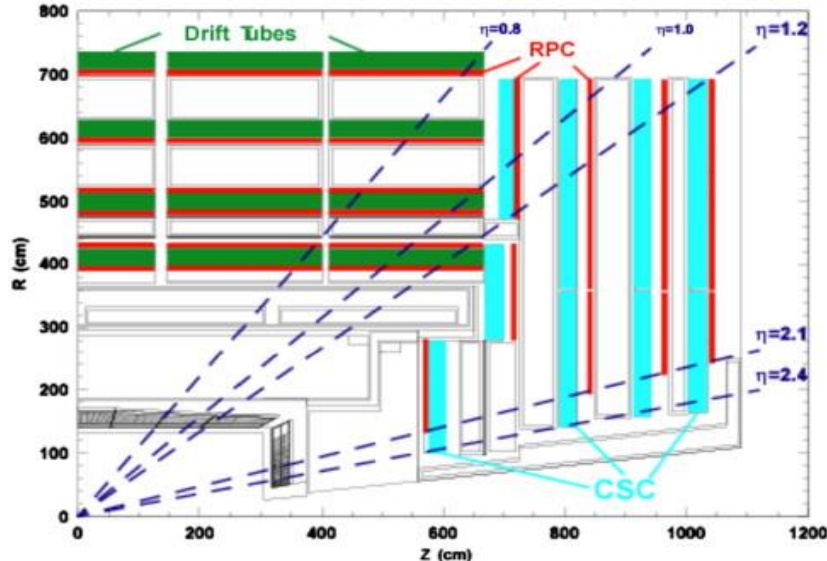


Figure 2.10 the position of the three different chamber designs

2.2.5 Magnet system

In order to make bending as large as possible on high-energy charged particles since the momentum resolution, the magnet system is needed. And unambiguous sign for muons is about 1 TeV with the momentum resolution of $\frac{\Delta p}{p} \approx 10\%$. The relative uncertainty on the momentum measurement is $\frac{\Delta p}{p} \propto \frac{p}{B}$. So the CMS magnet system is a superconducting solenoid providing the magnetic field of 3.8 Tesla at interaction point as listed in Table 2.1. The magnetic flux generated by the superconducting coil is returned via a 1.5 m thick saturated iron yoke. The tracker system, ECAL and HCAL are hosted within the magnet. The CMS magnet system consists of a superconducting coil, the magnet yoke, a vacuum tank and ancillaries such as cryogenics, power supplies and process controls.

Magnetic Field	4T
Inner Bore	5.9 m
Length	12.9 m
Number of Turns	2168
Current	19.5 kA
Stored Energy	2.7 GJ
Hoop Stress	64 atm

Table 2.1 The principal characteristics of the CMS solenoid magnet [15].

Chapter 3 Reconstruction of Physics Objects

3.1 Software Setup

Before the description of reconstruction, an introduction of the simulation process is given first and the algorithms used for the reconstruction of final state physics object are discussed in detail in Section 2.4. The CMS offline software is called CMSSW [25]; it is for the generation of simulated event, detector simulation, the reconstruction of collision or to run algorithms and analysis (ROOT) to get a good understanding of the particle collider's process. The flow chart of the analysis is shown in figure 3.1. CMSSW code is written in C++.

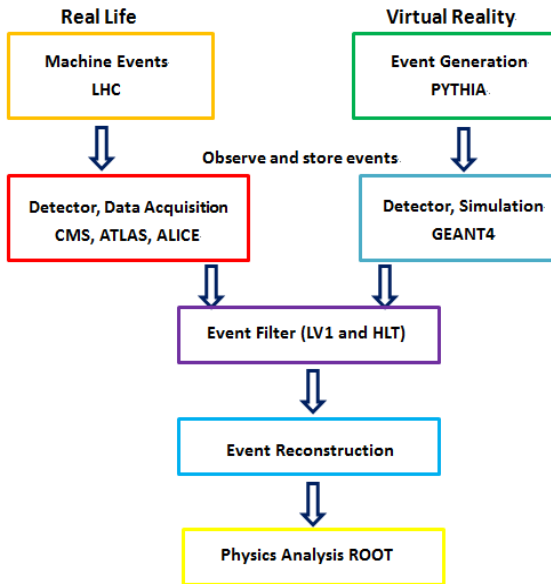


Fig.3.1 Overview of analysis flow in the CMSSW.

3.1.1 Event Generator

A typical event generator at the CMS experiment, PYTHIA [26], can be used to predict event rates, studies of complex particle process and simulate possible background. It can calculate the hard scattering process and resonance decays like the W boson into quarks or leptons. PYTHIA computes hadronization as well as several higher order effects: parton shower (initial and final state emission), multiple parton-parton interactions and underlying event.

3.1.2 Detector Simulation

The output of event generator is sent to GEANT4 [27] for detector simulation. We use GEANT 4 to simulate how particles propagate through space, how particles interact with the detector material, and the digital output of the detector response effects. CMS uses two software packages (Full Simulation [28] and Fast Simulation [29]) for detector simulation. The Fast Simulation directly produces high-level objects instead of hits, the interaction with sensitive detector components including resolution, so its speed is three orders of magnitude shorter than Full Simulation.

3.1.3 Trigger Simulation

Physics objects are generated by Monte Carlo generators and are propagated to detector simulation that includes the digitization. Finally the high level objects such as electron, photon and jets are reconstructed from those digitized samples. The details of the reconstruction of these high level objects are given in 2.4 Section.

Trigger is used to apply the selections to these physics objects. Trigger requirements are applied to both data and simulated events. The CMS system consists of two components, Level 1 Trigger (L1), and High Level Trigger (HLT), to decrease the background from proton-proton interaction/sec events (only 100events/sec can be stored but LHC can produce roughly 10^9 interaction/sec).

3.2 Final-State Objects Reconstruction

In this section, the physical objects that are measured in the CMS detector are described. Event from the $t^* \bar{t}^*$ production in the leptonic and hadronic channel will have the final state of the following objects: a photon, an electron or a muon, and at least 4 jets, of which two are b jets

Supercluster Reconstruction

The electromagnetic (EM) showers deposit their energy in several crystals in the ECAL. The adjacent ECAL crystals with the energy are grouped to clusters. The ECAL crystals are used to reconstruct the energy and the direction of photon or electron particle. Approximately 94% (97%) of incident energy of a single photon or electron is recovered in 3×3 (5×5) crystal array. Due to the strong magnetic field, bremsstrahlung electrons and converted photon from one initial electron or photon reach the ECAL with significant spread in ϕ direction. This spread of energy in

ϕ direction is clustered as a supercluster. Two cluster algorithms [30] are used.

The “hybrid” algorithm is used in the $\eta - \phi$ geometry of the barrel region. It starts from a crystal with transverse energy $E_T > E_T^{hybrid}$ (default value, 1GeV), a 1×3 domino of crystals are made in $\eta - \phi$ direction. If $E_{1 \times 3} > E_{wing}$, which is the threshold value of the 1×3 domino of crystal, the domino has been extended to 1×5 symmetrically around the seed crystal. This repeats N_{step} crystals in ϕ direction from the original seed until the dominoes with $E < E_{th}$ (default value, 0.1 GeV). The hybrid algorithm is shown in Figure 3.2.

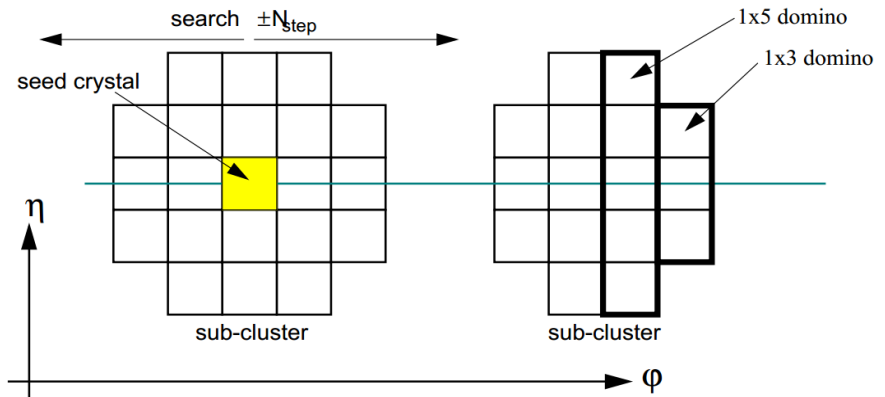


Fig. 3.2 Hybrid Supercluster Algorithm

The other “multi 5×5 ” algorithm is used in the endcap region. In multi 5×5 algorithm (“Island” algorithm), the center crystal of the 5×5 array crystal is the crystal with the highest E_T . It allows other seeds along the edge of original 5×5 array if the seeds are a local maximum when compared to neighboring crystals. Then the overlapping arrays of 5×5 crystals are joined together into one supercluster. The multi 5×5 algorithm is shown in Figure 3.3.

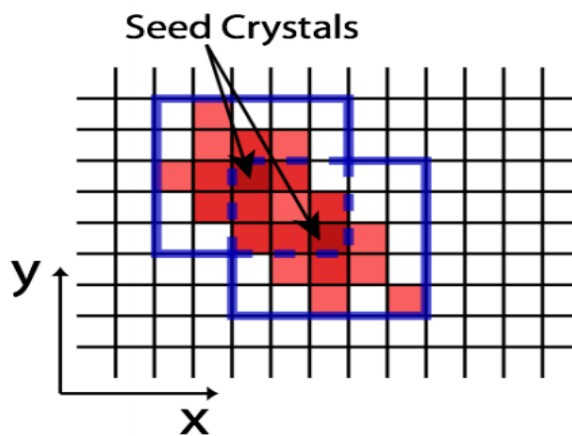


Fig. 3.3 Multi 5×5 Algorithm

Both of the location of a supercluster is determined by weighted average. The weighted equation of each crystal is:

$$x = \frac{\sum x_i \cdot w_i}{\sum w_i}, \quad w_i = \max[0, 4.7 + \log\left(\frac{E_i}{E_{sc}}\right)]$$

3.3 Photon Reconstruction

Photon energy calibration

Photon objects first are classified by whether they convert into electron-positron pairs before reaching the ECAL. The amount of crystals used to calculate photon energy is determined based on the energy ratio variable $r9 = E_{3\times 3}/E_{sc}$, which is defined as the energy in the 3×3 crystal window around the supercluster seed divided by the total energy of the supercluster. The tracker is in front of the ECAL, it leads to photon conversion into electron-positron pairs before touching the ECAL. The energy of the converted photons is spread along ϕ due to the magnetic field, so the small values of $r9$ are typical for converted photons. If $r9$ is more than 0.94 (0.95) for EB (EE) candidates, the cluster is classified as an unconverted cluster and the energy of a fixed 5×5 crystal energy around the seed crystal is used as the photon energy. Moreover, $r9$ is used to identify true photon: a π^0 will have a lower value when compared to an isolated photon.

3.3.1 Photon Selection Variables

When the reconstructed photon objects are obtained from the supercluster algorithms, a number of shower shape and isolation variables are calculated and used to highly suppress the background photons and enhance the purity of the photon sample. Anatomy of photon isolation is shown in Fig. 3.4. The selection variables include the following:

Shower Shape Variables

H/E is the ratio of energy deposited in HCAL to the energy in ECAL with radius $\Delta R = \sqrt{\Delta\eta^2 + \Delta\phi^2} = 0.15$ around a photon candidate. Typically, signal photon has a value < 0.05 . This variable is useful to reject hadrons since hadrons deposit most energy to HCAL whereas photons deposit almost all their energy to ECAL.

$\sigma_{i\eta i\eta}$ is the size of the electromagnetic cluster measured along the η direction and computed with logarithmic weights [31]:

$$\sigma_{i\eta i\eta}^2 = \frac{\sum (\eta_i - \bar{\eta})^2 \omega_i}{\sum \omega_i}, \quad \bar{\eta} = \frac{\sum \eta_i \omega_i}{\sum \omega_i}$$

$$\omega_i = \max(0, 4.7 + \log\left(\frac{E_i}{E_{5*5}}\right))$$

Where E_i and η_i are the energy and pseudorapidity of the i th crystal within a matrix of 5×5 crystals cluster seed like figure 4.3. The E_{5*5} and $\bar{\eta}$ are the sum of the energy and the weighted average of the pseudorapidity in the matrix. The 4.7 value controls the smallest fractional energy, so the crystals in the cluster containing more than 0.1% of the cluster energy contribute to the position measurement. Because the energy spread in the φ direction only, the value of $\sigma_{i\eta i\eta}^2$ tends to be smaller for single isolated photon including converted photon.

Isolation Variables

Iso_{trk} is the scalar sum of the transverse momentum of track originating from the primary interaction vertex and lying in a hollow cone of size $\Delta R = 0.4$ around the photon momentum direction, An inner cone $\Delta R = 0.02$ and a rectangular strip of $\Delta\eta \times \Delta\varphi = 0.015 \times 0.4$ are excluded to avoid including the momentum of conversion tracks.

Iso_{ECAL} is the sum of the transverse energy collected by the electromagnetic calorimeter crystals in a cone $0.06 < \Delta R < 0.4$ around the photon direction. The contribution due to conversion is also removed by excluding the sum of transverse energy in a $\Delta\eta \times \Delta\varphi = 0.04 \times 0.4$. In addition, the energy in a crystal must satisfy $|E| > 80$ MeV to reduce electronics noise.

Iso_{HCAL} is the sum of the energy collected in the HCAL towers in a cone $\Delta R = 0.4$ around the photon momentum direction, excluding an inner cone of radius $\Delta R = 0.15$, which corresponds to the region used to measure the H/E ratio.

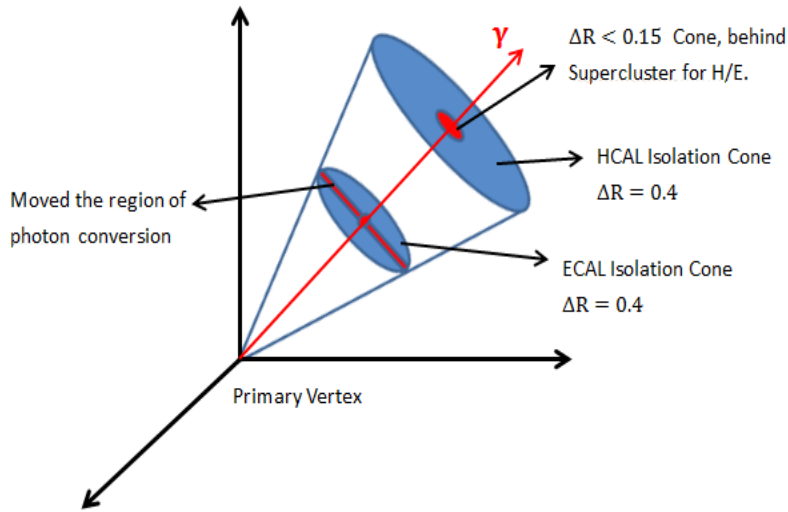


Fig. 3.4 Sketch of Photon Isolation to study of what else is in the detector.

3.3.2 Track Finding for Conversion

The variables of converted photons also help rejecting π^0 . Because the sum of the P_T on the tracks is the same as the energy deposited in the ECAL, the isolation photons have the E_T/P_T ratio around one. If the fake two photons from π^0 decay, it would not total convert to electron pairs. In this case, the energy collected in the ECAL will be more than the photon momentum measured by the tracker. Candidates with E_T/P_T larger than a threshold value are likely to be background.

Pair production is only possible if the energy of photon exceeds twice the rest mass of the electron and the pair must be created near a nuclear electric field. Because the rest mass of the photon is zero, the positron and electron exhibit a tendency to move parallel in the same direction as photon. Then the CMS magnetic field causes the electron and positron tracks to bend along the ϕ direction. The bremsstrahlung photons emitted by the electrons as they traverse the inner tracker material are also spread along ϕ . Therefor we use supercluster which collect energy along the ϕ direction as the starting point for conversion reconstruction.

The energy of the ECAL and the magnetic field is an initial guess for the track momentum to give a first rough estimate path. A sketch of inward-outward track is shown in Figure 3.5. The inward track (1) is seeded from a basic cluster in the ECAL supercluster (blue) and hits in the outermost three tracker layers. The outward track (2) is then built using the innermost hit of the inward track as a hypothesis for the conversion vertex. [32, [33, [34] Oppositely-charge pairs of tracks are combined to form conversion candidates.

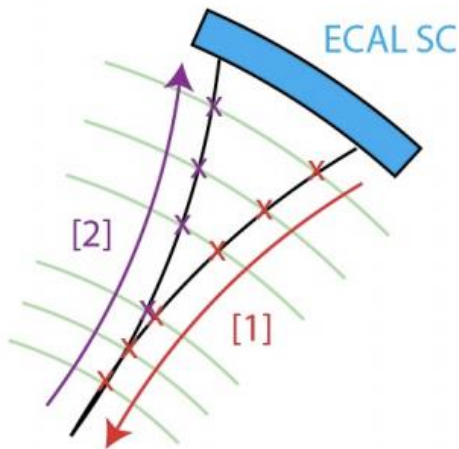


Fig. 3.5 Sketch of inward-outward track.

3.4 Electron Reconstruction

As an electron passes through the CMS detector, it produces a track in the tracker system, as well as the energy deposits in the electromagnetic calorimeter. Therefore electron candidates are reconstructed by matching tracks and energy clusters. There are two reconstruction algorithms: the “ECAL-driven” method and the “tracker-driven” method. The first algorithm starts from energy deposits in the ECAL, and the other algorithm starts from a reconstructed track.

Both methods need to consider fact that of electron not only ionizes the medium but may suffer energy loss via the radiation of photon, which is the process of bremsstrahlung. Electron tracking relies on the Gaussian Sum Filter (GSF) [35, [36] algorithm to deal with the problem of energy loss. With the GSF track fit, the change of curvature caused by the electron bremsstrahlung and different momentum estimates are obtained at the inner and outer track position (energy loss $f(\text{brem}) = (P_{IN} - P_{OUT})/P_{IN}$, see Figure 3.6).

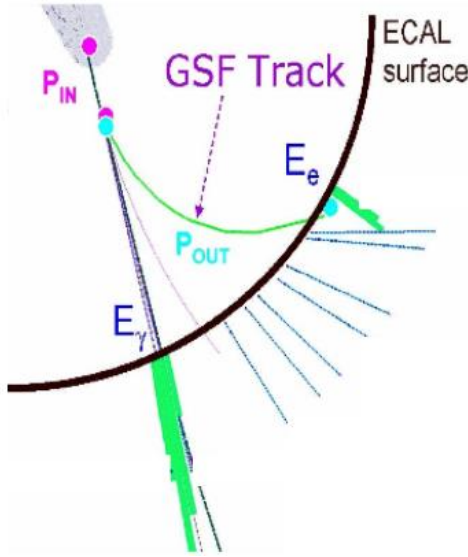


Figure 3.6 GSF used for Bremsstrahlung emission in the tracker

ECAL-driven Electron Seeding

The ECAL-driven seeding is well suited for isolated and high- P_T electrons ($P_T > 10$ GeV) and it is based on ECAL information. The reconstruction of ECAL energy is described in section 2.3. The supercluster must match with a track to reconstruct the electron. A possible trajectory is estimated by extrapolating the probable position of tracker hits from the supercluster's position. A hit is sought along trajectory in inner or middle pixel layer within a window. Once a hit is found, a second hit is sought along that trajectory in the next pixel layer.

Tracker-driven Electron Seeding

The Track-drive seeding was developed to deal with low- P_T from bremsstrahlung and non-isolated electrons within jets. First, a track is obtained by using the Kalman Filter algorithm [42]. Then, we try to match track to calorimeter and search for nearby energy clusters. All the tracks are tested with an acceptable (E/P) ratio and the cluster closest in $\eta - \phi$ space to the track is chosen.

3.4.1 Electron Selection Variables

The reconstructed electron candidates from the ECAL-driven and tracker-driven seeding methods are preselected to reduce the rate of jets faking electrons. In ECAL-driven seeding method, the $E_T > 4$ GeV and $H/E < 0.15$ are required at seeding level. In addition to this selection, the criteria for good track-supercluster matching are applied. In case of tracker-driven, the multivariate analysis is used.

The $\Delta\eta$ and $\Delta\phi$ matching angular distance between the supercluster and the

track are used. $|\Delta\eta_{in}| \equiv |\eta_{sc} - \eta^{extr}_{in}| < 0.02$ and $|\Delta\phi_{in}| \equiv |\phi_{sc} - \phi^{extr}_{in}| < 0.15$, where $\eta_{sc}(\phi_{sc})$ is the energy weighted position in $\eta(\phi)$ of the supercluster and $\eta^{extr}_{in}(\phi^{extr}_{in})$ is the $\eta(\phi)$ coordinate of the position of closest approach to the supercluster position, extrapolating from the innermost track position and direction.

To distinguish electrons from jets electron identification is applied. The cluster shower shape variable $\sigma_{i\eta i\eta}$ (see the section 3.3.1) discriminates between electron energy depositions and showers developed by photons. The $\sigma_{i\eta i\eta}$ together with the ratio between hadronic and electromagnetic energy ($H/E < 0.12$ in Barrel, $H/E < 0.1$ in endcap) and track matching ($\Delta\eta$ and $\Delta\phi$) are all called electron identification variables.

3.4.2 Photon Conversion Rejection

There are large multiple scattering, bremsstrahlung and high photon conversion rates occurred in the CMS tracking system. Electrons from photon conversions are non-negligible background to prompt electrons. The Missing Hits and Vertex fit Prob variables are used to reduce the contamination coming from converted photons:

MissingHits is the number of missing hits in the innermost tracker layers for the electron track. The prompt electron's trajectory starts from the primary proton-proton collision vertex. Therefore, there are no missing hits in the inner tracker layers like Figure 3.7; we use this variable at inner tracker layers to reject electrons from photon conversion.

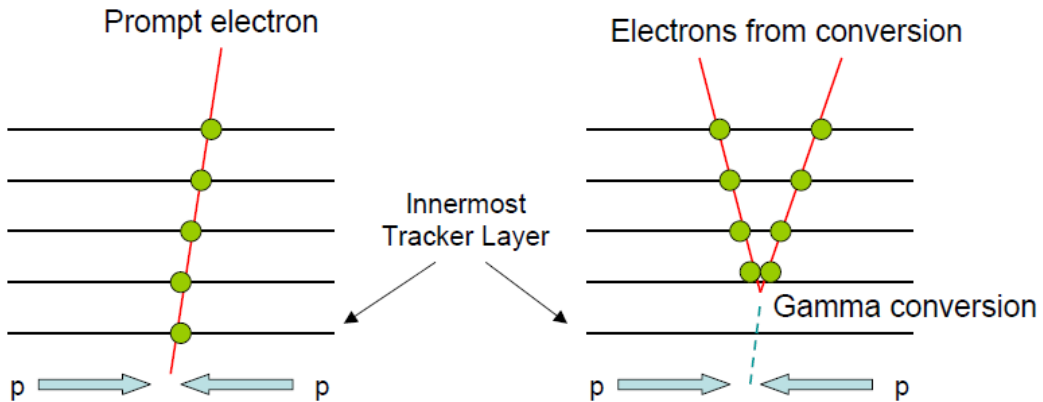


Figure 3.7 MissingHits. The left hand side is a prompt electron which usually has a hit on the innermost track layer. The right hand side is the converted photon which often does not have hits on the first layer.

3.5 Muon Reconstruction

Muons are reconstructed using the Muon System and Tracker information in three steps. First, the blue region in Fig. 3.9: a pattern-recognition algorithm is run in the Muon System to find seeds for the reconstruction of tracks. Second, the green region in Fig. 3.9: it is reconstruction of the track inside the Muon System by using Kalman-filter technique. The collection of muon in this step is called Standalone Muon. In the third step, the orange region in Fig. 3.9: it is the reconstruction of the track combining the information from the Tracker and the Muon System. The muon object obtained in this step is called Global Muon.

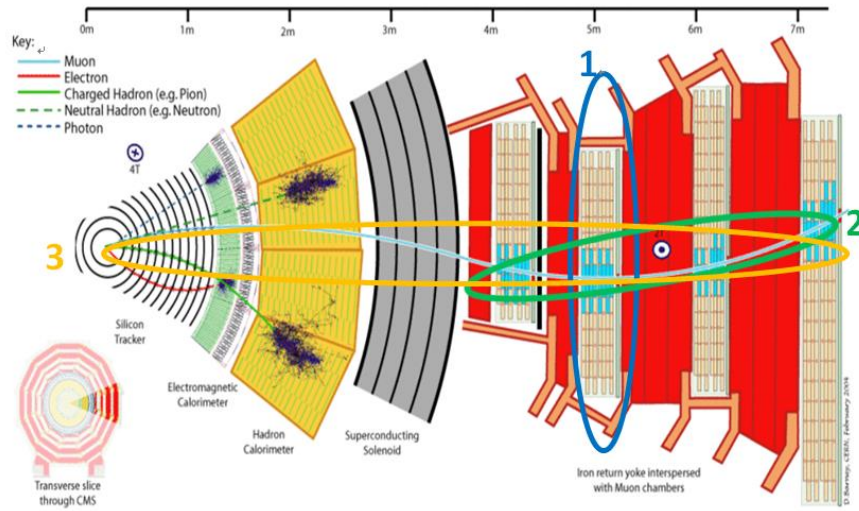


Figure 3.8 The muon reconstruction is divided into three steps.

The first step is in blue region, the second step is in green region and the third step is in orange region.

3.6 Jet Reconstruction

The definition of jet is not unique and there are several approaches available for jet clustering. The anti- k_T algorithm [37] is described in this section. In the anti- k_T algorithm high- p_T particles are clustered first, contrary the k_T algorithm clusters soft particles first. The algorithm based on the following two distance measures:

- d_{ij} is the distance between two particles i and j: $d_{ij} = \min(k_{Ti}^{-2p}, k_{Tj}^{-2p}) \frac{\Delta y^2 + \Delta \phi^2}{R^2}$ with $\Delta y^2 = (y_i - y_j)^2$ and $\Delta \phi^2 = (\phi_i - \phi_j)^2$, where k_{Ti} , y_i and ϕ_i are the transvers momentum, rapidity and azimuth of particle i respectively. R is the jet

radius parameter that determines the jet size; CMS uses $R=0.5$ and $R=0.7$. The parameter p sets the power of the transvers momentum scale; anti- k_t uses $p = -1$.

- d_{iB} is the distance from particle i to the beam: $d_{iB} = k_{Ti}^{-2p}$.

The anti- k_t algorithm is both collinear and infrared safe algorithm. Collinear safety means the hard jets (or a stable cones) has a collinear splitting, i.e. collinear splitting ($\theta \sim 0^\circ$), see figure 3.10. In this case, nearly collinear particles are clustered as same jets. Infrared safety means the soft emission particle does not affect clustering results drastically, see figure 3.11.



Figure 3.9 Collinear safety

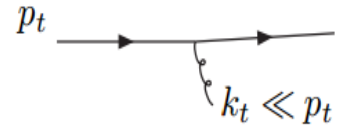


Figure 3.10 Infrared safety

The algorithm merges particles until no particle j is found that content with $d_{ij} < d_{iB}$. If d_{iB} is the smallest distance, the i is considered a complete jet and this jet is removed from the list of particles for cluster. Figure 3.12 shows the anti- k_t algorithm result with injected soft particle to illustrate infrared safety.

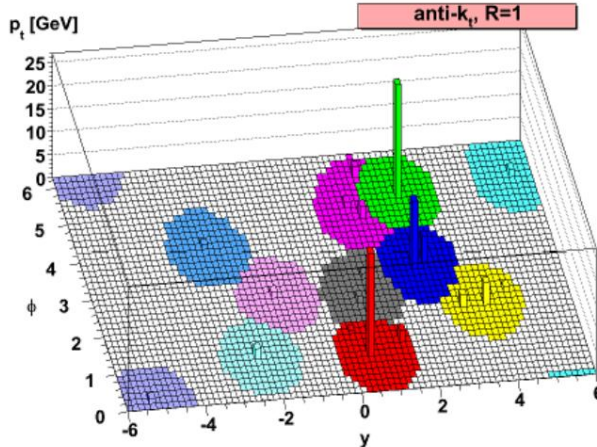


Figure 3.11 Colored areas represent anti- k_t clustered jets.

Jet Selection Criteria

The leading jet must have a minimum transvers momentum of 30 GeV. The leptons in the event are also classified as jets so we need to separate them from the real jets. If the distance in the $\eta - \phi$ plane between the jet axis and the leptons is greater than 0.3, this jet is removed from the jet collection. To discard those unwanted jets, a set of loose jet identification criteria are also used.

Chapter 4 Analysis

4.1 Monte Carlo Simulation of Background

The background processes belonging to events with a similar or the same final state are from W boson production with associated jets and single top quarks via the electroweak interactions. All these processes modes can lead to a final state with a charged lepton, a neutrino, and jets in events. Further Standard Model background with a similar final state is like the di-bosons (WW, WZ, ZZ) production. Single top or anti-top quarks are produced by three different mechanisms, s-channel, t-channel, and tW-channel production. We also computed ttbar pair hadron production with a heavy boson like $t\bar{t}W$, $t\bar{t}Z$ backgrounds and new process such as pp->ttG.

The cross section of the sample is a fixed quantity dependent on the process generated. The cross sections of the physics processes are summarized in Table 4.1 and Table 4.2. In order to perform the Monte Carlo background having the same luminosity as data, it is necessary to weight the MC sample to correspond to data luminosity. The weighting factor should be: weight = (cross-section*Luminosity)/Number of entries.

Process (generator)	σ (pb)	equivalent Lumi (/pb)
QCD Pt-15to30	988287420.0	0.000366
QCD Pt-30to50	66285328.0	0.006109
QCD Pt-50to80	8148778.0	0.047247
QCD Pt-80to120	1033680.0	0.800754
QCD Pt-120to170	156293.3	5.650114
QCD Pt-170to300	34138.15	8.419788
QCD Pt-300to470	1759.549	178.475848
QCD Pt-470to600	113.879	2834.795849
QCD Pt-600to800	26.9921	9758.521938
QCD Pt-800to1000	3.550036	84962.237003

Table 4.1 List of processes and cross sections used for the normalization of the Monte Carlo samples.

Table 4.2 List of processes and cross sections used for the normalization of the Monte Carlo samples.

Process (generator)	σ (pb)	equivalent Lumi (/pb)
TTJets	227.0	29846.409692
Single top, t-channel	56.4	420.425532
Single top, s-channel	3.79	68385.224274
Single top, tW-channel	11.1	43209.909910
Single tbar, t-channel	30.7	61313.322476
Single tbar, s-channel	1.76	70259.659091
Single tbar, tW-channel	11.1	44276.666667
DYJets	3512.103509	6638.635490
DiPhotonJets	75.39	15285.701021
WGToLNuG	461.6	10251.499133
ZGToLLG	132.6	49589.713432
WJetsToLNu	35640.0	1412.505836
WW	69.9	43199.127325
WZ	33.21	252226.136706
ZZ	8.4	1076496.666667
ttW	0.232	837202.586207
ttG	1.444	7575007.692308
ttZ	0.2057	1011754.982985

The simulated background samples are generated with MadGraph [38], PYTHIA, or POWHEG [39, [40, [41]. We generate the SM background using MadGraph for $pp \rightarrow tj$, $pp \rightarrow \gamma\gamma j$, $pp \rightarrow ZG \rightarrow \ell\ell G$, $pp \rightarrow Wj \rightarrow \ell\nu$ and Drell-Yen process. The contribution from hadronisation programs are simulated with PYTHIA. The production of single top quarks events are generated with POWHEG.

The background distribution of the reconstructed signal for the $t\bar{t}\gamma\gamma$ final state coming from the pair production of spin- $\frac{3}{2}$ quarks with $\sqrt{s} = 8TeV$ is shown in Fig.4.1.

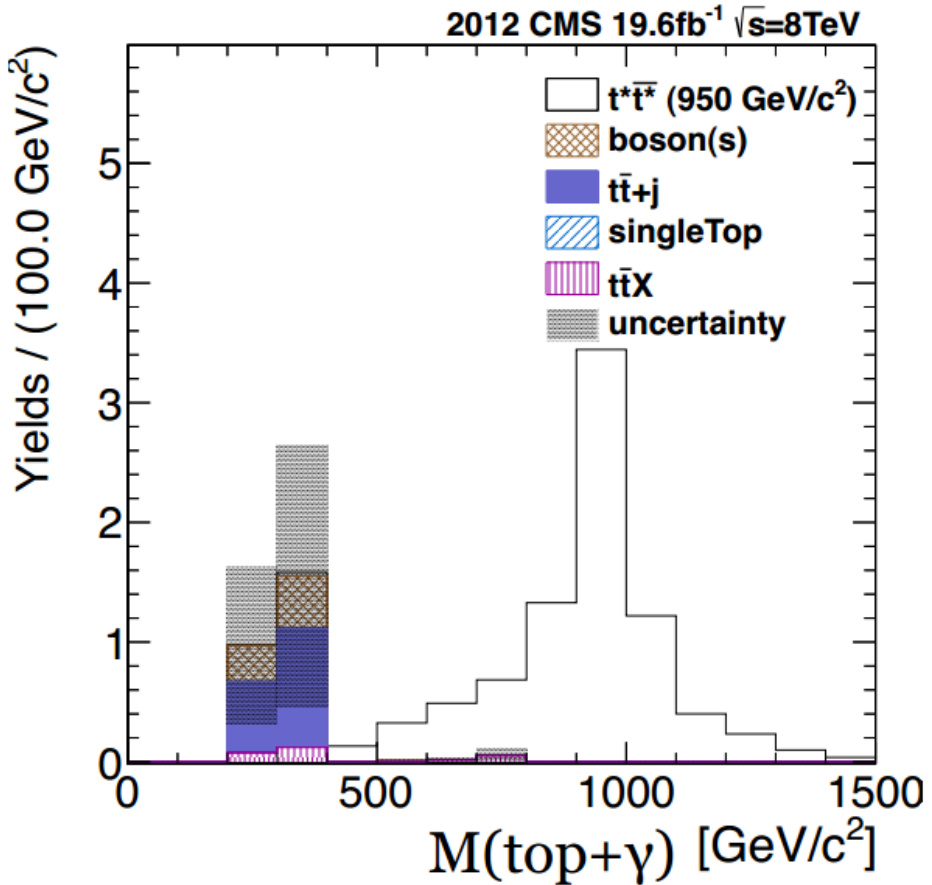


Fig.4.1 Distribution of the reconstructed invariant mass.

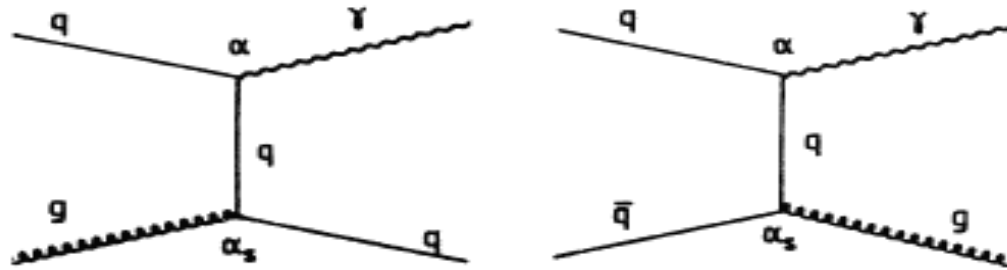
4.1.1 Estimation of Inclusive Photon

We use a data driven background estimation in t^* analysis. Because a jet has probability to be identified as photon in the t^* event, we can use fitting method to distinguish them in the data set. We can derive purity ($\frac{N_\gamma}{N_{jet \rightarrow \gamma} + N_\gamma}$) from fitter, and calculate probability of fake photon from jet ($\frac{N(1-purity)}{N_{jet}}$) where N is the total number of jet passing photon ID cut. We let the data to multiply this fake rate value, and then we can estimate the contribution from this background MC sample. This section first describes the χ^2 fitting method and how to use inclusive photon data to demonstrate the χ^2 fitting method. The second method, extended likelihood, is also discussed in this section.

Inclusive Isolated Photon Production

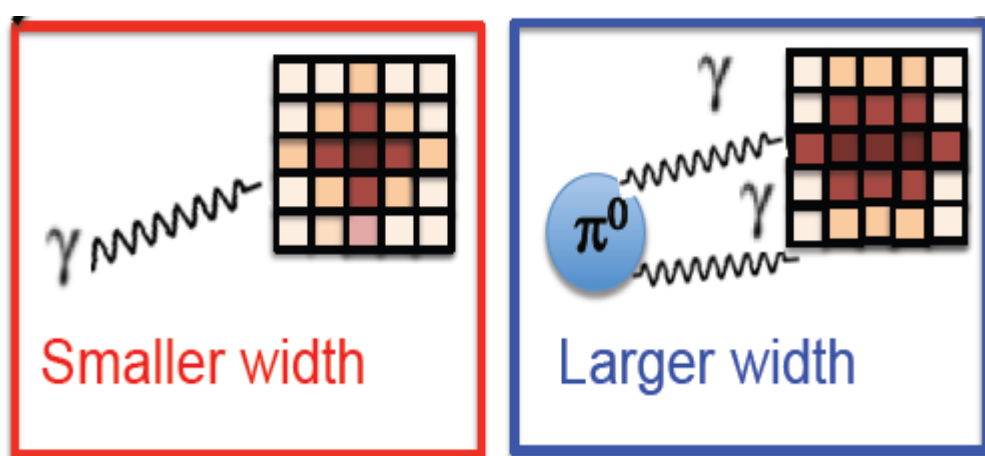
Photon is expected to be produced by quark-antiquark annihilation and Compton process $qg \rightarrow q\gamma$ (Fig. 4.2). The dominant mechanism at the LHC is the Compton process in the hard scattering.

Figure 4.2 Feynman diagram of the leading order photon process



The isolated prompt photon yield is estimated by fitting discriminating variable $\sigma_{i\eta i\eta}$ (the definition is shown in section 3.3.1). The trajectory of converting photon ($\gamma \rightarrow e^+ e^-$) is not affected by the magnetic field in η , while for photons produced in hadron decays with opening angle, $\pi^0 \rightarrow \gamma + \gamma$, its $\sigma_{i\eta i\eta}$ distribution tends to have long tail. The $\sigma_{i\eta i\eta}$ distribution therefore provides a good indication of the modeling of background (Fig 4.3).

Figure 4.3 Transverse shower shapes with crystals. The left hand side is the signal figure, and the right hand side is the background figure.



χ^2 Fitter

The Chi-squared method is based on the statistics of the Chi-squared function:

$$\chi^2 = \sum_{i=1}^n \frac{(y_i - F(x_i, a))^2}{\sigma_i^2}$$

It assumes the number of counts in each bin will have a Gaussian distribution with an expectation value. In total of n measurements, the y_i are the individual measurements like data values, and the predicted value of the model is $F(x_i, a)$ where a is the purity parameter. The standard error of each measurement is the σ_i .

The sum of squares is characterized by the estimated variance of the fit. It can be estimated by χ^2/N_{dof} and it should be close to 1.0 for a good fit. If the difference between observed and expected value is large, it means the model is a poor fit to the data.

χ^2 Distribution

The probability distribution for χ^2 (Fig. 4.4) can be obtained from:

$$P(\chi^2; n) = \frac{2^{-n/2}}{\Gamma(n/2)} \chi^{n-2} e^{-\chi^2/2}$$

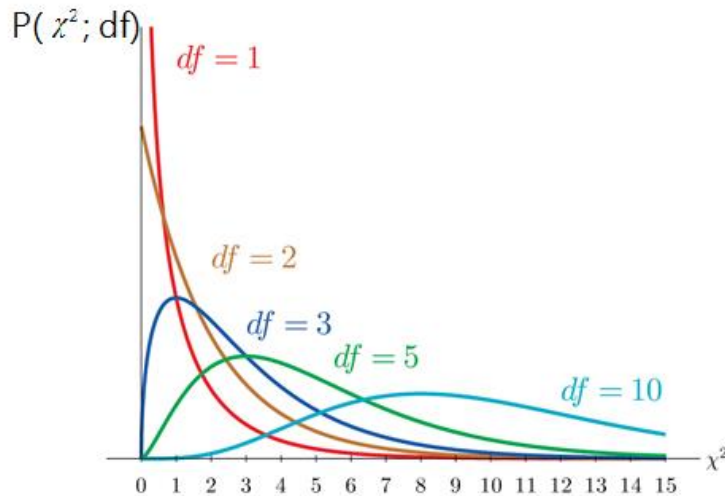


Fig.4.4 Several χ^2 probability distributions for different degree of freedom. df is the number of degree of freedom. For large n, the distribution tends to Gaussian.

Where $\Gamma(x)$ is the standard gamma function. The distribution depends on the number of degrees of freedom (N_{dof} , n) which is the sum of bin of distribution minus the number of free parameters. It has the properties that the mean value n and variance $2n$. Thus expectation value of χ^2 per degree of freedom is roughly one.

$$\begin{aligned}
\langle \chi^2 \rangle &= \langle \sum_{i=1}^n \chi_i^2 \rangle \\
&= \sum_{i=1}^n \langle \frac{(x_i - \mu_i)^2}{\sigma_i^2} \rangle \\
&= \sum_{i=1}^n 1 \\
&= n
\end{aligned}$$

The other useful information for any degree of freedom is

$$F_n(\chi_{obs}^2) = P_n(\chi^2 > \chi_{obs}^2) = \int_{\chi_{obs}^2}^{\infty} P(\chi^2, n) d\chi^2$$

The percentage area in the tail of χ_{obs}^2 distribution gives an indication of the agreement. For example, the expected mean value of χ^2 is 20, if we got a very small value of χ^2 like 3.3 ($P(\chi^2 > 3.3; N = 20) = 99.999\%$) which means only 0.001% chance of getting such a small value. It is likely errors not estimated correctly.

Likelihood Fitter

An extended maximum likelihood fit is performed over the $\sigma_{i\eta i\eta}$ distribution and the measured data $\sigma_{i\eta i\eta}$ distribution is compared to Monte Carlo expectations. The signal shape and QCD background are derived from MC simulations. Parameterizing these signal and background templates we construct probability density functions (p.d.f.) events to be used in the likelihood. The term $\mathcal{L}(\bar{x}; \bar{p})$ determines the signal yield N_s and background N_b by comparing the distribution of $\sigma_{i\eta i\eta}$ in the data with signal and background p.d.f's $L_s(x)$ and $L_b(x)$. The observed total number event N is not fixed and can fluctuate by Poisson statistics with mean value μ which is from $\mathcal{L}(\bar{x}; \bar{p})$ prediction. The mean value we got here is the total expected number of signal and background ($\mu = N_s + N_b$).

$$\begin{aligned}
\bar{\mathcal{L}}(\bar{x}, N; \bar{p}, \mu) &= P(N; \mu) \cdot \mathcal{L}(\bar{x}; \bar{p}) \\
\bar{\mathcal{L}}(\bar{x}, N; \bar{p}, \mu) &= \frac{\mu^N}{N!} e^{-\mu} \cdot \prod_{i=1}^N f(x_i; \bar{p})
\end{aligned}$$

We observe a mixture of the two event types (e.g., signal and background): $L_s(x), L_b(x)$. Each of pdf depends on some measured quantity like momentum and energy. Here we use $\sigma_{i\eta i\eta}$. Our goal is to estimate N_s and N_b from signal fraction \bar{p} . Let $N_s = p\mu$, $N_b = (1-p)\mu$.

$$f(x; N_s, N_b) = \frac{N_s}{N_s + N_b} L_s(x) + \frac{N_b}{N_s + N_b} L_b(x)$$

To interpret variance estimation, we did Taylor expand $-\ln(L)$ around minimum:

$$\begin{aligned} -\ln L(x) &= -\ln L(\hat{x}) - \ln L'(\hat{x})(x - \hat{x}) - \frac{1}{2} \ln L''(\hat{x})(x - \hat{x})^2 \\ &= -\ln L_{max} - \ln L''(\hat{x}) \frac{(x - \hat{x})^2}{2} \\ &= -\ln L_{max} + \frac{(x - \hat{x})^2}{2\sigma_x^2} \end{aligned}$$

The distribution of $L(x)$ is Gaussian, and we can know the errors from the log likelihood function, $\ln L(p \pm \sigma) = \ln L_{max} + \frac{1}{2}$. The log likelihood has increased by 0.5 from its minimum and this value corresponds to 1σ . In MINUIT package, the default value to take variance value is one, so doubling log likelihood is necessary to avoid getting large variance value.

$$-\ln(\mathcal{L}) = 2 * \left(-\sum \ln(F(x, p)) - N \ln(\mu) + \mu \right)$$

We determine the number of events in the function by maximum likelihood or minimum $-\ln(L)$. It is easier to maximize $\ln(L)$ rather than L since $\ln(L)$ turns the product into a summation. And then we put them in $-\ln(L)$ function because of convenience (using the MINUIT package from CERN program library) and dropped out the constant term($\ln(N!)$):

Testing Fitter with Pseudo Experiments

We use pseudo-experiments, toy MC, to check if the χ^2 and extended maximum likelihood fitter returns the proper expected value. We construct a set of 1000 pseudo data and each pseudo data is made randomly from signal and background templates. The number of pseudo data is given by random Poisson

fluctuation. The quantity to check the quality of the fit results is $\text{Pull} = (P_{fit} - P_{input})/\sigma_{fit}$. If everything is OK, the pull distribution is a standard normal distribution. Pull mean is 0 (Gaussian distribution centered at zero) if there is no biased. Pull sigma is 1 (Gaussian's standard deviation) if the statistical uncertainty estimate is no biased. Figure 4.5 shows the pull sigma with a function of pt range. Figure 4.6 shows the pull mean value with a function of pt range.

4.1.2 Photon Purity

The signal sample was derived from PYTHIA simulation sample, photon-jet event MC. The background shape is extracted from data side-band region by requiring $2 < ISO_{trk} < 5$ and keeping all other selections the same as signal criteria. The χ^2 fitting results (Fig.4.7) are obtained by separating the photon candidates into several pt bins. The expected number of signal and background from 25GeV to 200 GeV 12-pt bins and the shape of the likelihood function are shown in Fig.4.8.

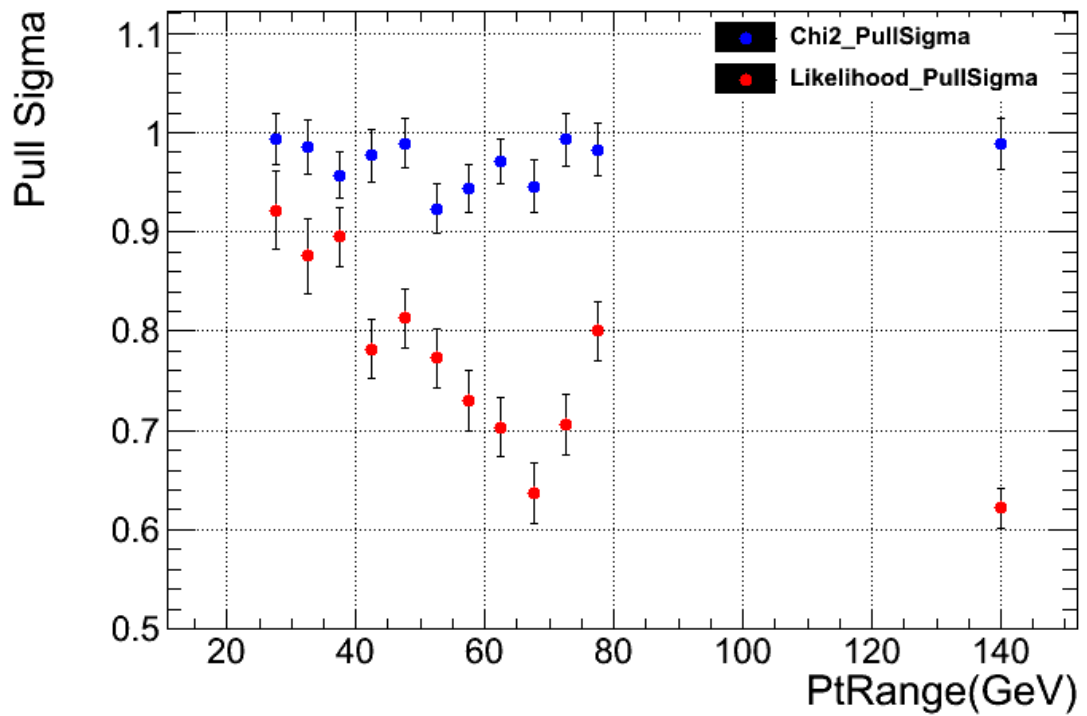


Figure 4.5 Sigma of the pull distributions in pseudo-experiments.

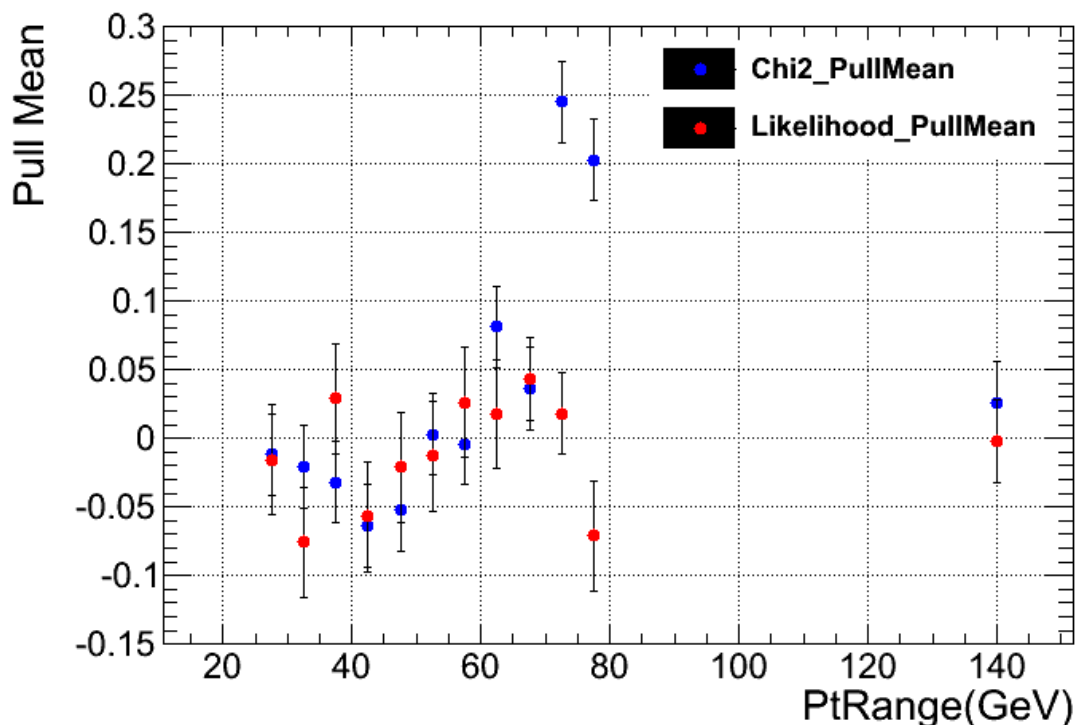


Figure 4.6 Average of the pull distributions in pseudo-experiments.

Figure 4.7: Fitting shower shape ($\sigma_{in in \eta}$) variable with 12 Pt bins in Barrel region. Pt 25-30 GeV, Pt 30-35 GeV, Pt 35-40 GeV, Pt 40-45 GeV, Pt 45-50 GeV, Pt 50-55 GeV, Pt 55-60 GeV, Pt 60-65 GeV, Pt 65-70 GeV, Pt 70-75 GeV, Pt 75-80 GeV, Pt 80-200 GeV.

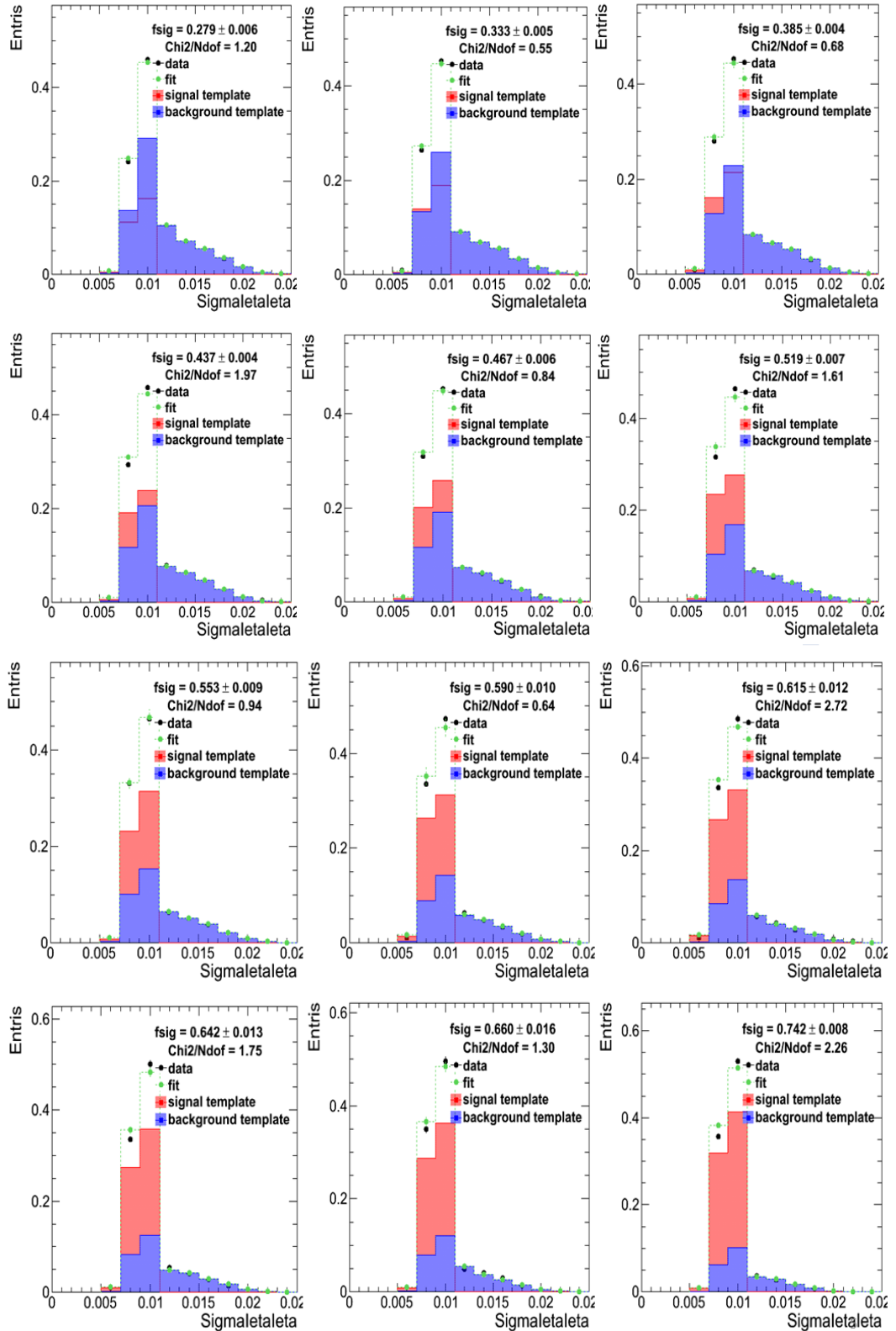
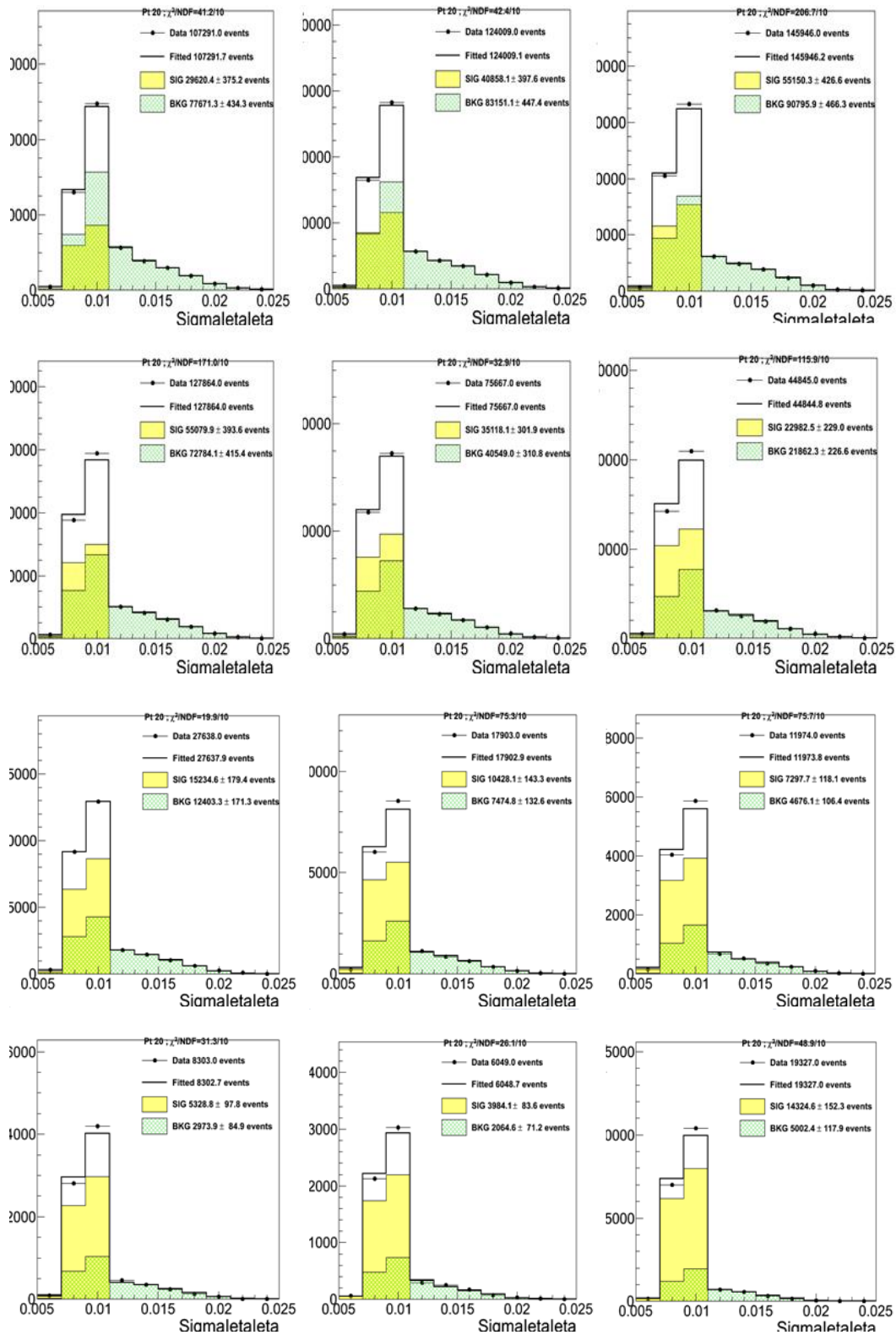


Figure 4.8: Fitting shower shape ($\sigma_{in in}$) variable with 12 Pt bins in Barrel region.
 Pt 25-30 GeV, Pt 30-35 GeV, Pt 35-40 GeV, Pt 40-45 GeV, Pt 45-50 GeV, Pt 50-55 GeV,
 Pt 55-60 GeV, Pt 60-65 GeV, Pt 65-70 GeV, Pt 70-75 GeV, Pt 75-80 GeV, Pt 80-200
 GeV.



4.2 Mass χ^2 Sorting

The reconstruction of the invariant mass of t^* pair is given by total energy and momentum of the final state objects, i.e. two photon, the charged lepton and neutrino, and four jets. This section described the way to reconstruct the $m_{t^* \bar{t}^*}$, which involves two steps. First, the leptonic W decays into lepton and neutrino pairs. The neutrino escapes the detector undetected and the total sum of the transverse momenta is not zero. Only the transverse component of neutrino can be obtained from the missing transverse energy in the experiment, and the longitudinal component needs to be calculated using a W boson mass constraint. Second, if more than four jets appear in one event, jets need to be selected that most likely originate from the $t^* \bar{t}^*$ decay chain. The χ^2 sorting method is a way to choose four jets to correctly reconstruct $m_{t^* \bar{t}^*}$. Among these four jets, we have to decide which two jets to assign to the W hadronic decay, which jet to assign to the top hadronic decay and which jet to assign to the top leptonic decay.

4.2.1 Longitudinal Momentum of the Neutrino

There is no difficulty in determining neutrino's transverse momentum p_{\perp}^{ν} which can be procured from missing momentum within the event. However, particle acted upon by unbalanced energy in beam pipe direction; hence they have nonuniform motions in z direction. One can calculate unknown longitudinal momentum of the neutrino is by exploiting the known mass of the W boson of $m_W = 80.4$ GeV to construct the equation of the longitudinal momentum of the neutrino.

The sum of lepton's and neutrino's four momenta squared should be equal to W boson's invariant mass squared:

$$P_W^2 = M_W^2 = (P_{\nu} + P_{\ell})^2 = P_{\nu}^2 + P_{\ell}^2 + 2P_{\nu}P_{\ell}$$

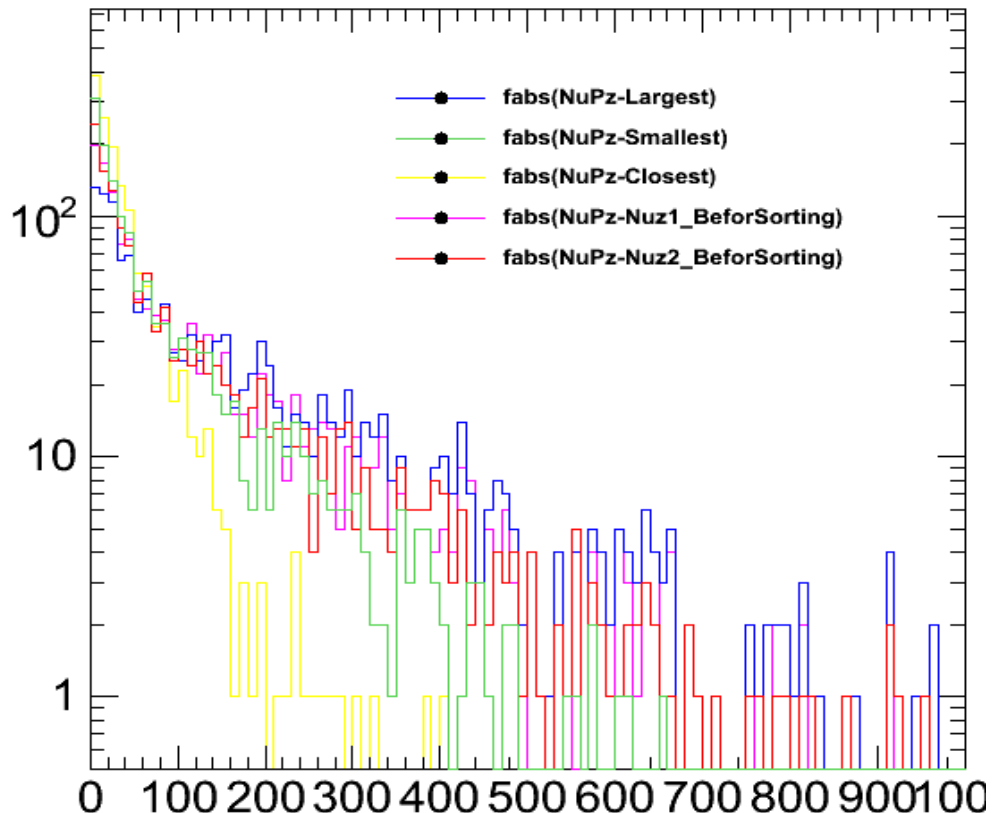
There are two solutions, called nuz1 and nuz2, for p_{\parallel}^{ν} that would be got from above equation. This ambiguity can be determined by comparing MC theory value, choosing one which is always close to the value of generation level.

In order to know which solution is the best, we test the following values:

$$|NuPz - \alpha|, |NuPz - \beta|, |NuPz - P_z^{\nu}|, |NuPz - Nuz1_{BeforeSorting}|, |NuPz - Nuz2_{BeforeSorting}|.$$

where $\alpha = \text{largest}(\text{nuz1}; \text{nuz2})$, $\beta = \text{smallest}(\text{nuz1}; \text{nuz2})$, and $P_z^\nu = \text{closest}(\text{nuz1}; \text{nuz2})$. The beforeSorting means before the selection of larger or smaller one. Then we compare the various results by superimposing the five plots and applying a log scale on the y-axis of the plot. (Fig.4.9)

Figure 4.9 The plots show only positive values, given by the various $\text{abs}(\text{NuPz} - \text{XXX})$.



Another important indication is to do the fractions of num/den. The num means counting events if $\text{smallest}(\text{nuz1}; \text{nuz2})$, $\text{largest}(\text{nuz1}; \text{nuz2})$ are respectively equal to $\text{closest}(\text{nuz1}; \text{nuz2})$ condition is satisfied. The den means counting the number of events in which at least one neutrino satisfied MC matching .

$$f_{\text{smallest}} = \text{num_smallest(excluding case where nuz1=nuz2)}/\text{den} = 736/1369 = 0.537$$

$$f_{\text{largest}} = \text{num_largest(excluding case where nuz1=nuz2)}/\text{den} = 337/1369 = 0.246$$

$$f_{\text{same}} = \text{num_same_solution(those cases where nuz1=nuz2)}/\text{den} = 296/1369 = 0.216$$

4.2.2 Mass Resolution

If N ($N \geq 4$) jets are reconstructed in one event, this group of four jets has twelve possibilities of jet-quark association. In addition, there are two solutions to account for the longitudinal momentum of the neutrino as discussed above. To find a correct assignment, a χ^2 sorting is adopted. It is not a fit, but a way to evaluate all possible jets combinations and to select the combination with the lowest χ^2 value.

The total χ^2 is defined by four terms, hadronic W , hadronic top, leptonic top, hadronic t^* and leptonic t^* :

$$\chi^2 = \frac{|W_{jj} - 80.4\text{GeV}|^2}{\sigma_{W_{jj}}^2} + \frac{|top_{wjj+b} - 173.5\text{GeV}|^2}{\sigma_{t_{wjj+b}}^2} + \frac{|top_{wlv} - 173.5\text{GeV}|^2}{\sigma_{t_{wlv}+b}^2} + \frac{|t^*_{t_{wjjb}+\gamma} - t^*_{t_{wlvb}+\gamma}|^2}{\sigma_{t_{lep}}^2 + \sigma_{t_{had}}^2}$$

Each term has the form:

$$\chi^2 = \frac{|X_{mass} - X_{MC}|^2}{\sigma_{MC}^2},$$

X_{mass} is the measured value of mass and X_{MC} is the expected value of mass with width σ_{MC} from simulated $t^*\bar{t}^*$ events. We fit the hadronic W mass with Gaussian at range from 70 to 90 GeV, the hadronic top mass with Gaussian at range from 115 to 195 GeV and the hadronic t^* mass with Gaussian at range from 750 to 850 GeV. (see Fig. 4.10) All reconstructions of fitting masses are shown in Appendix.

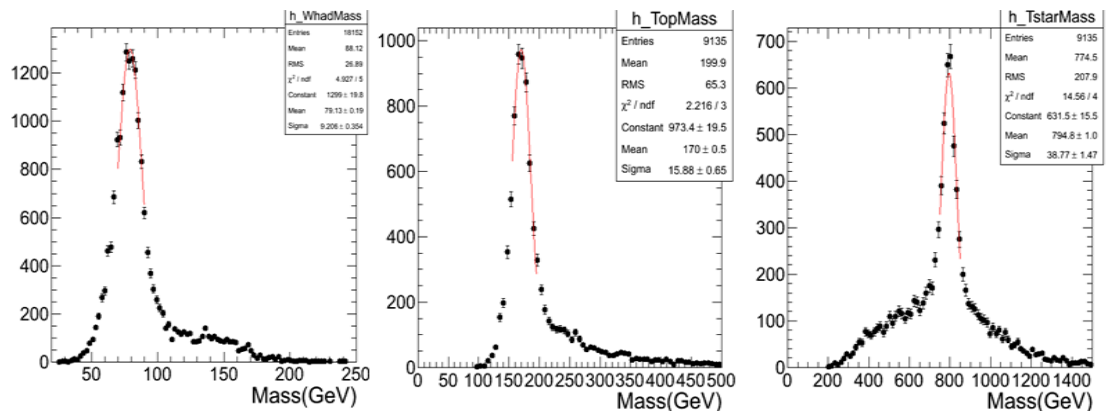


Figure 4.10 Mass resolutions. The Left-handed is the hadronic W mass, the middle

one is the hadronic top mass, and the right handed is the hadronic t^* mass.

A correct jet-parton association is defined by requiring that all jets are correctly matched to the same decay chain. The widths of the reconstructed masses are determined by fitting Gaussian function. The widths of hadronic channel and leptonic channel results with various signal samples are fit to a constant, getting the constant resolution for these signal masses (Fig. 4.11, 4.12, 4.13). We extracted $\sigma_w = 9.3 \pm 0.1 \text{ GeV}/c^2$, $\sigma_{top} = 16.5 \pm 0.1 \text{ GeV}/c^2$ and $\sigma_{t^*} = 31.6 \pm 0.28 \text{ GeV}/c^2$. For hadronic t^* plot, we also fit the mass resolution to a first-order polynomial: mass resolution = $0.04 \cdot \text{mass} + 7.29$ (Fig. 4.13 right hand side).

In the reconstruction of leptonic decay channel, the neutrino's longitudinal momentum is selected the closer in absolute value to the longitudinal momentum of the gen level value one. The results are shown in Figure 4.14, 4.15. We extracted $\sigma_{top} = 22.4 \pm 0.27 \text{ GeV}/c^2$ and $\sigma_{t^*} = 31.6 \pm 0.43 \text{ GeV}/c^2$. For leptonic t^* plot, the fit the mass resolution to a first-order polynomial: mass resolution = $0.03 \cdot \text{mass} + 12.4$ (Fig. 4.16).

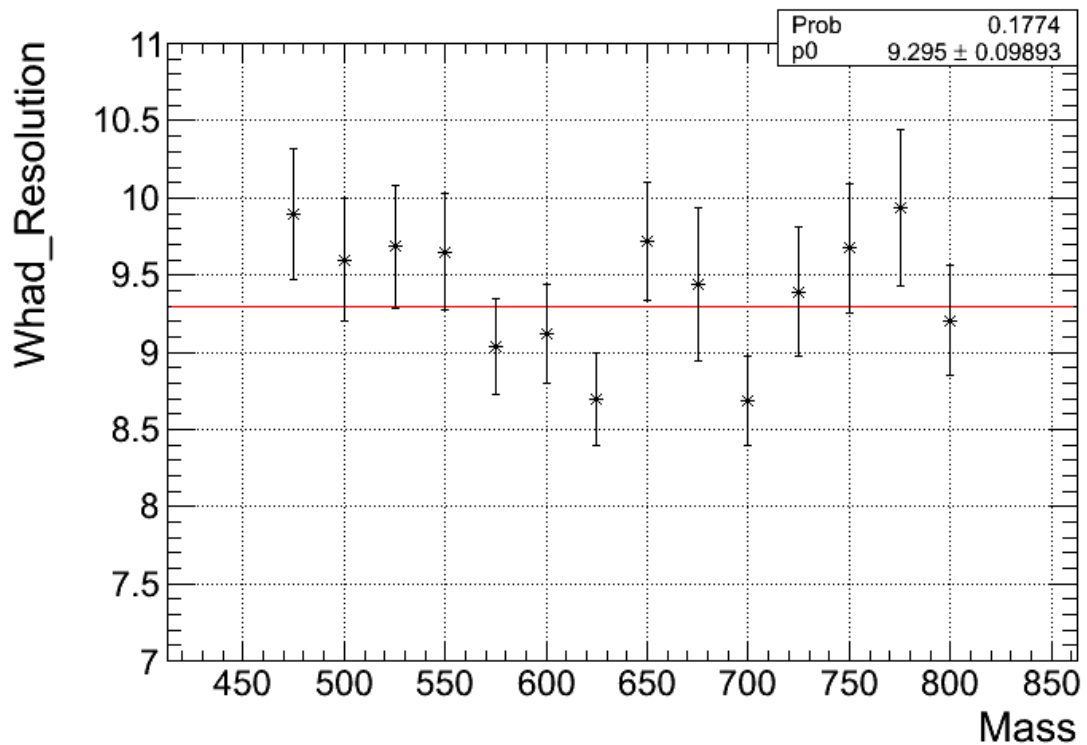


Fig. 4.11 Hadronic W's mass resolution as a function of signal mass.
The mass distribution of hadronic W boson for each t^* mass is reconstructed.

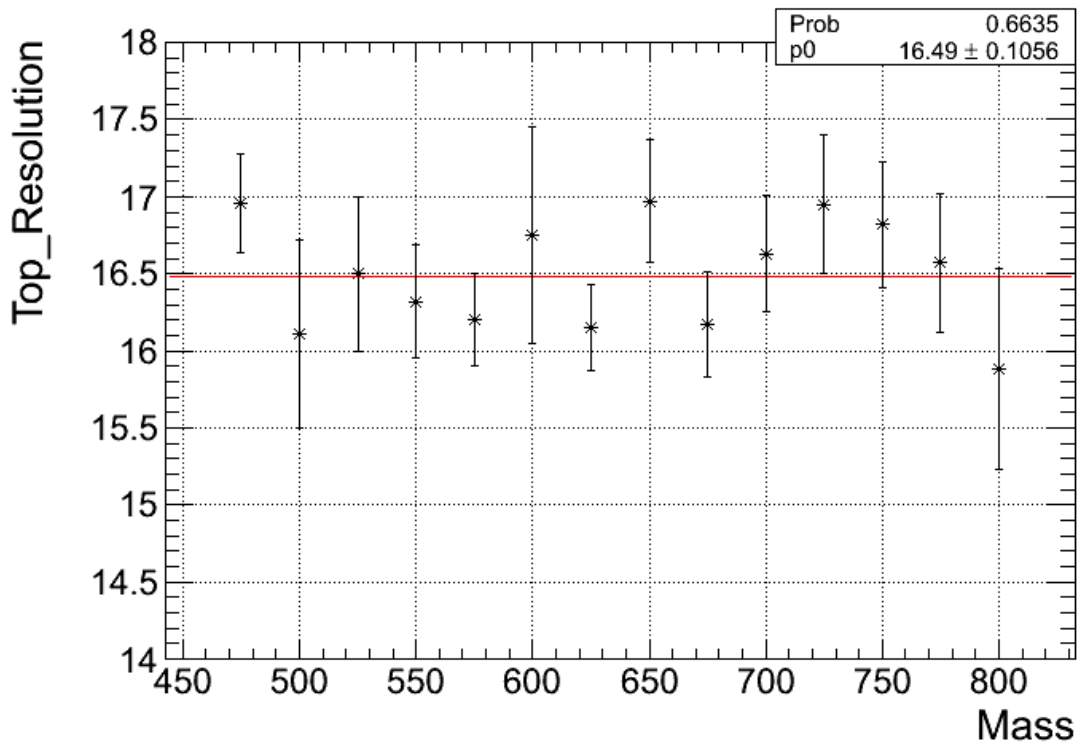


Fig. 4.12 Hadronic top's mass resolution as a function of signal mass.
The mass distribution of hadronic top for each t^* mass is reconstructed.

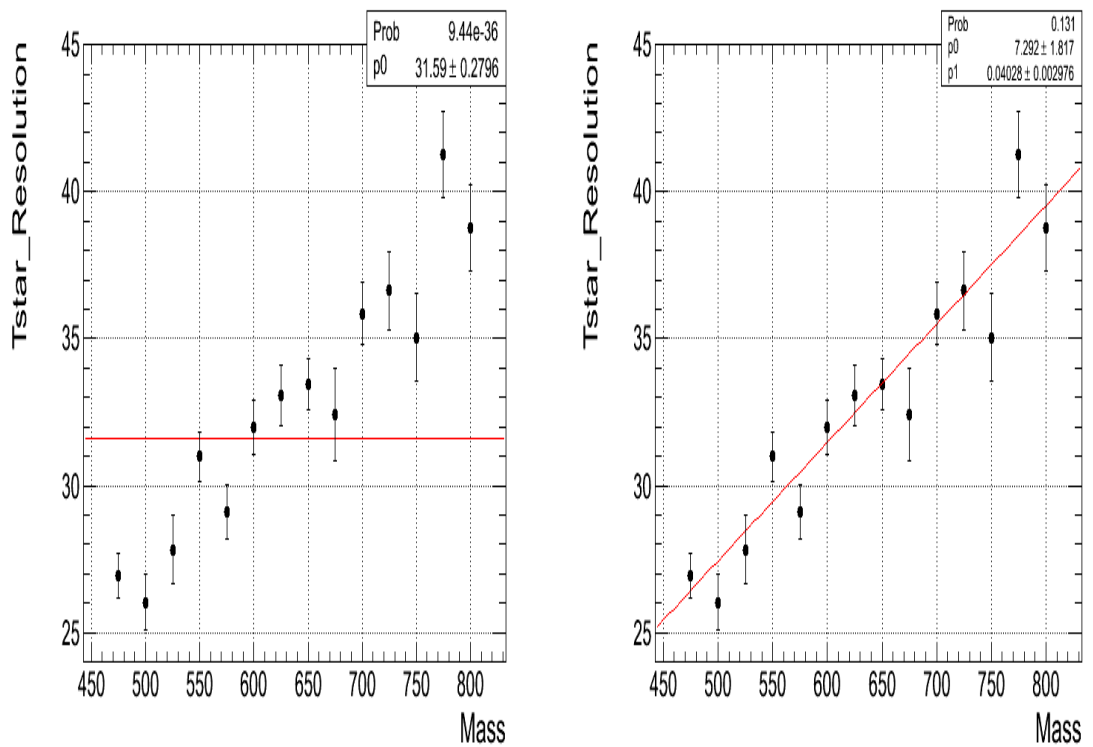


Fig. 4.13 Hadronic t^* mass resolution as a function of signal mass.
Fitting constant with 31.6 (left hand side), Fitting the mass resolution to a first-order polynomial $0.04 * \text{Mass} + 7.29$ (right hand side).

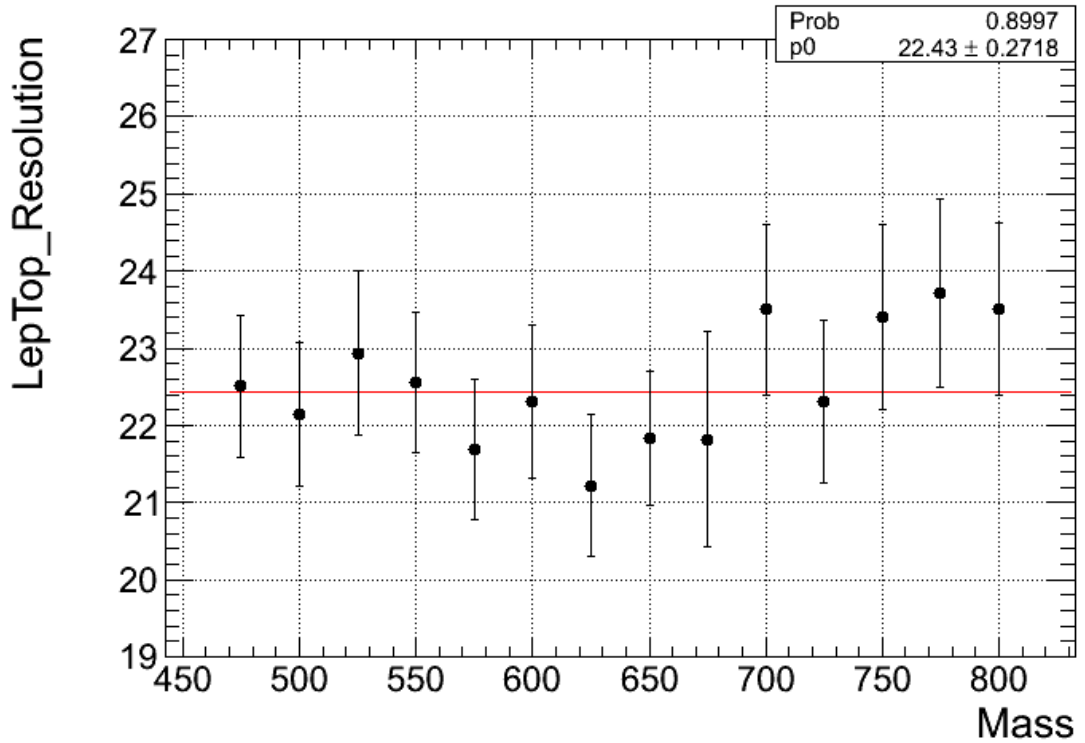


Fig. 4.14 Leptonic top mass resolution as a function of signal mass.
The mass distribution of leptonic W boson each t^* mass is reconstructed.

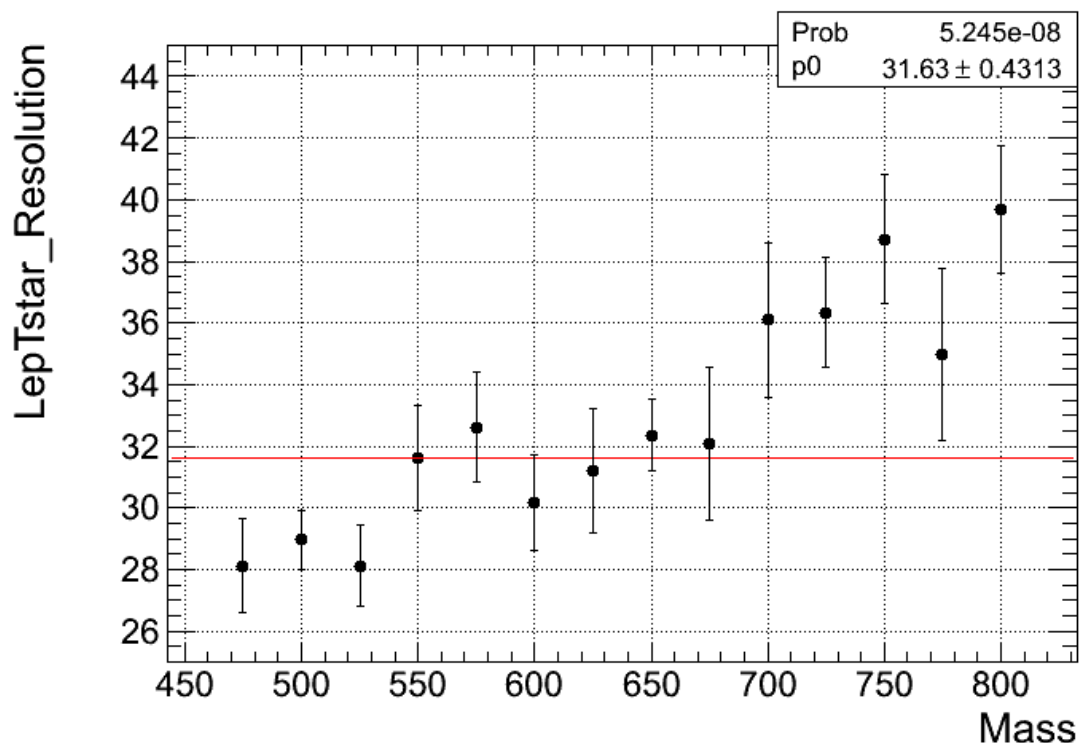


Fig. 4.15 Leptonic t^* mass resolution as a function of signal mass.
The mass distribution of leptonic top for each t^* mass is reconstructed.

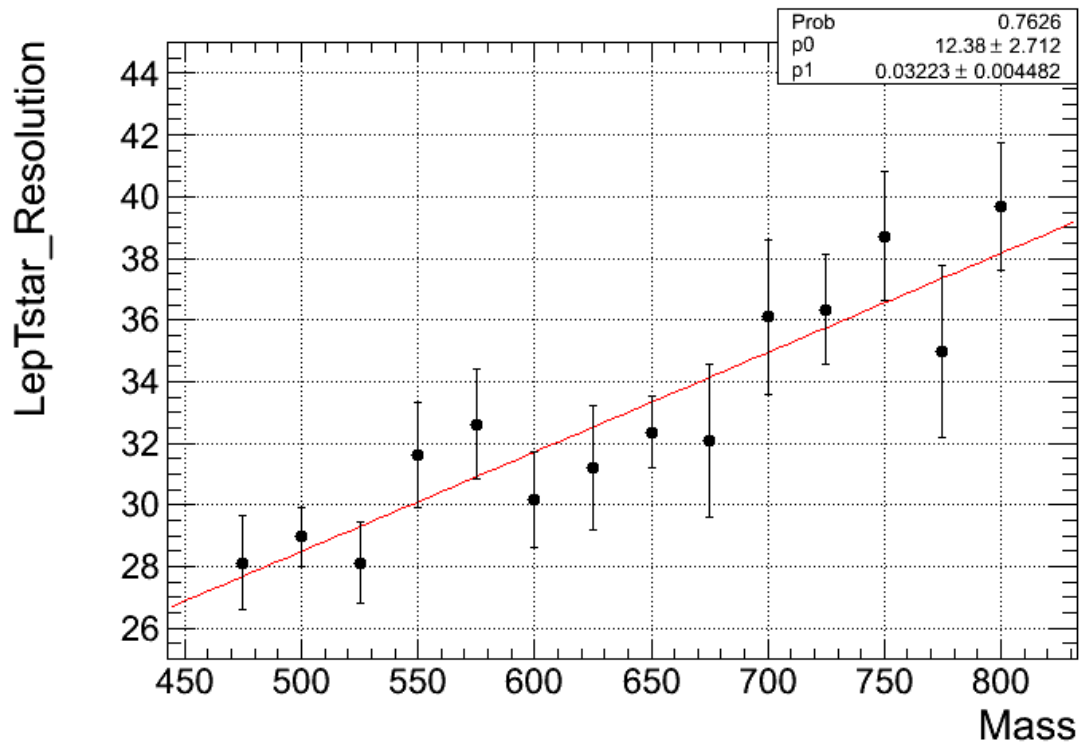


Fig. 4.16 Leptonic t^* mass resolution as a function of signal mass.

Fitting the mass resolution to a first-order polynomial $0.03 * \text{Mass} + 12.4$.

Chapter 5 Conclusion

Many extensions of the Standard Model predict the existence of new particles t^* in the TeV scale. In this paper we studied the production of KK particles in bulk RS models in the $t_R^* \rightarrow t\gamma$ channel at the LHC. The analysis was based on the final state of the $t^*\bar{t}^*$ system with one charged lepton, i.e. either a muon or an electron, four jets, and two photon. In addition, we selected the smaller value among the ambiguity solutions of the neutrino's longitudinal momentum by calculating the conservation of four momenta. With 19.6 fb^{-1} of data recorded with the CMS detector at a centre-of-mass energy of 8 TeV at the LHC, we now consider the 100% branching ratio of $t_R^* \rightarrow t\gamma$ and derive the exclusion limits up to about 990 GeV/c^2 at 95% confidence level.

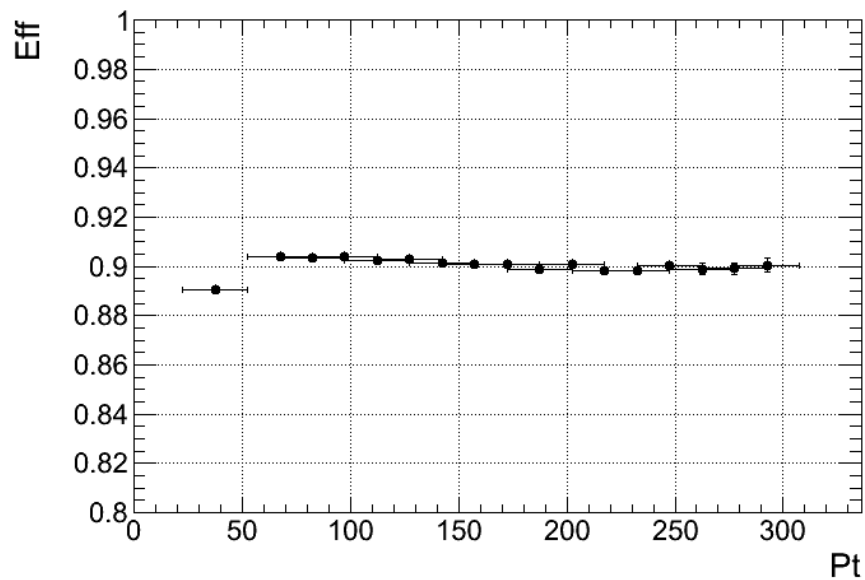
All selected decay products were associated to final state particles and the goodness of association was tested by a χ^2 sorting method. Therefore we studied the mass resolution of the decay products for reconstruction of $t^*\bar{t}^*$ events. We extracted $\sigma_w = 9.3 \pm 0.1 \text{ GeV}/c^2$, $\sigma_{top} = 16.5 \pm 0.1 \text{ GeV}/c^2$ and $\sigma_{t^*} = 31.6 \pm 0.28 \text{ GeV}/c^2$ in hadronic decay channel and $\sigma_{top} = 22.4 \pm 0.27 \text{ GeV}/c^2$ and $\sigma_{t^*} = 31.6 \pm 0.43 \text{ GeV}/c^2$ in leptonic decay channel. In this study, the Drell-Yan process and the W+Jet dominate as the major background contributions. Therefore the next step is studying the fake rate. We are going to try to use χ^2 fitter to estimate the fake photon from jet. Completion of the estimation work is expected to be at the end of this year.

Appendix

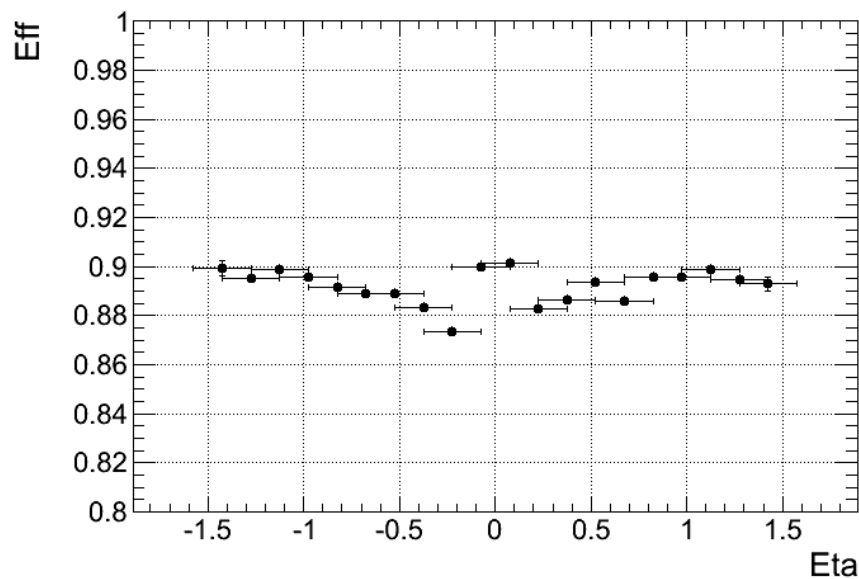
Efficiency

The photon selection efficiency is defined as the ratio of the number of photon that passes identification to the number of total photon in Barrel region

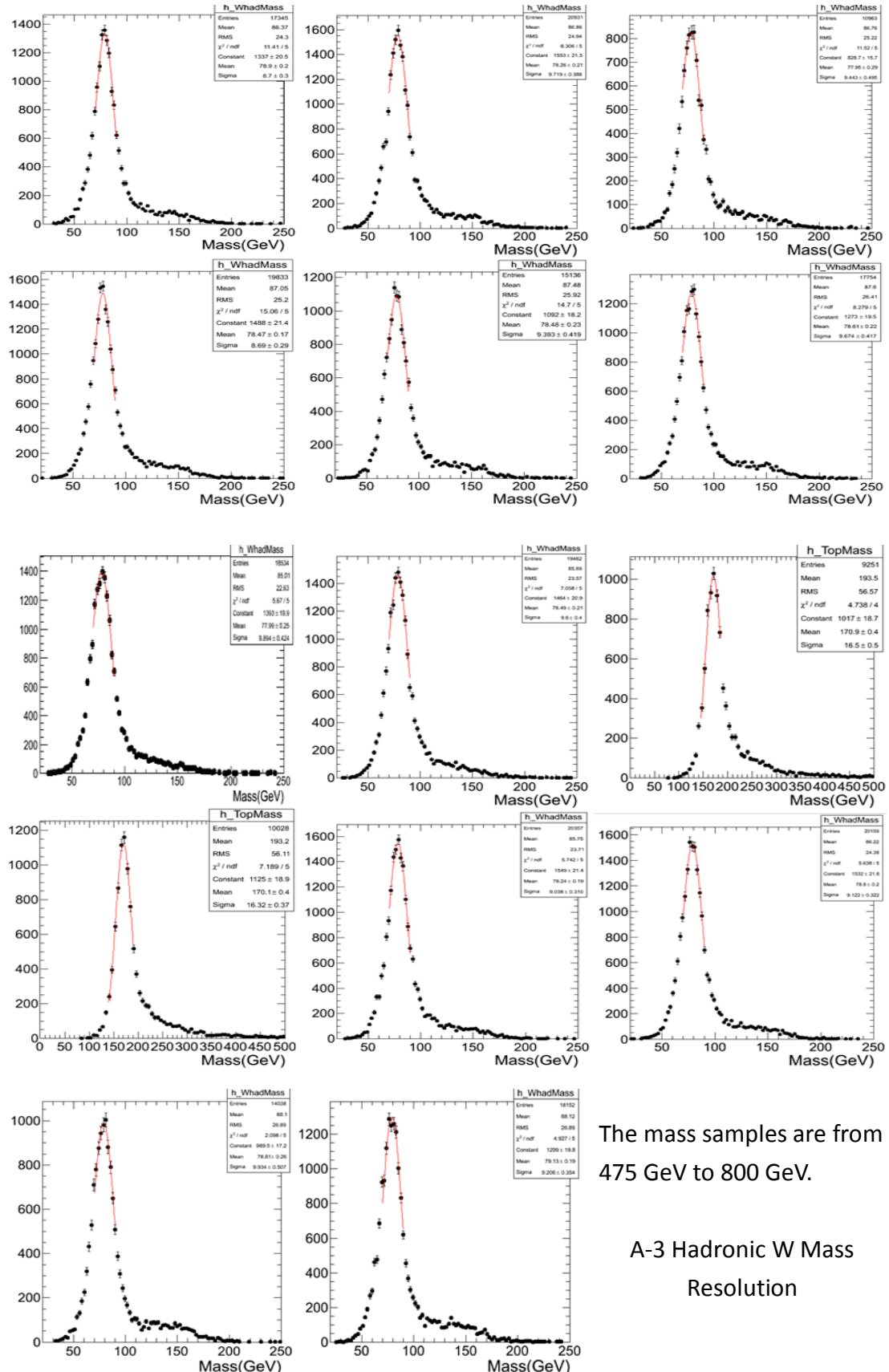
A-1 Signal efficiency with a function of pt.



A-2 Signal efficiency with a function of eta.



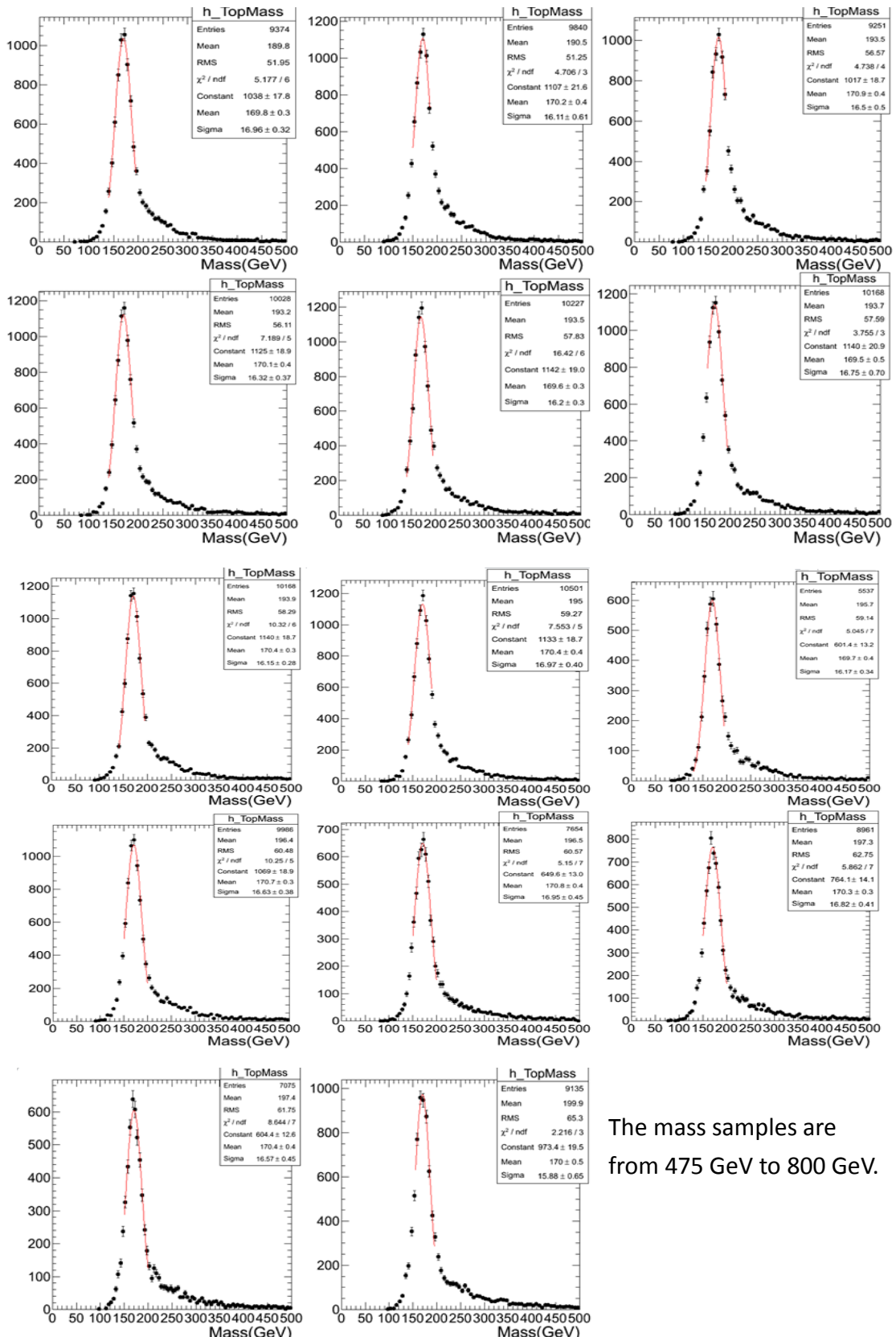
Mass Resolution



The mass samples are from 475 GeV to 800 GeV.

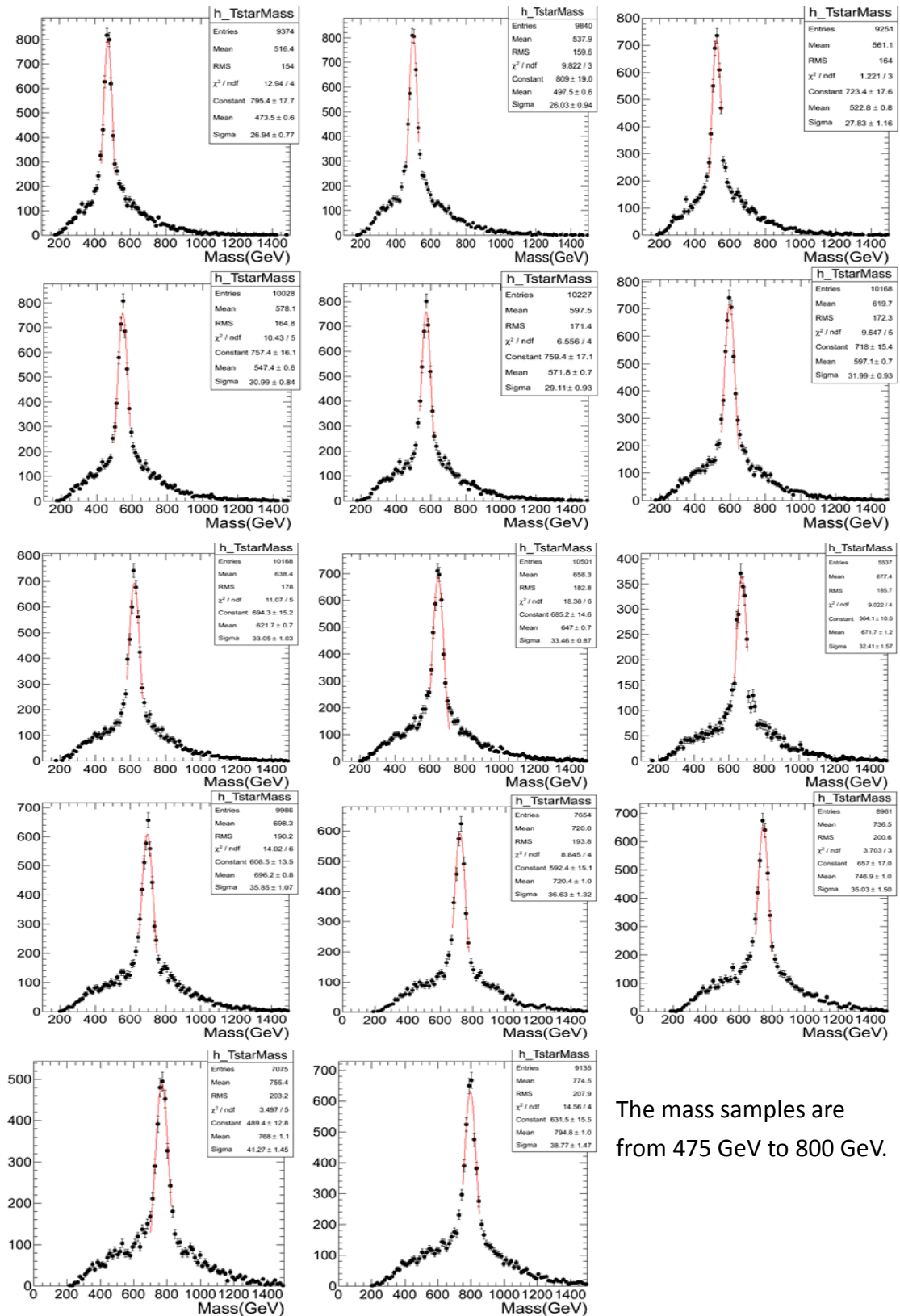
A-3 Hadronic W Mass Resolution

A-4 Hadronic top Mass Resolution



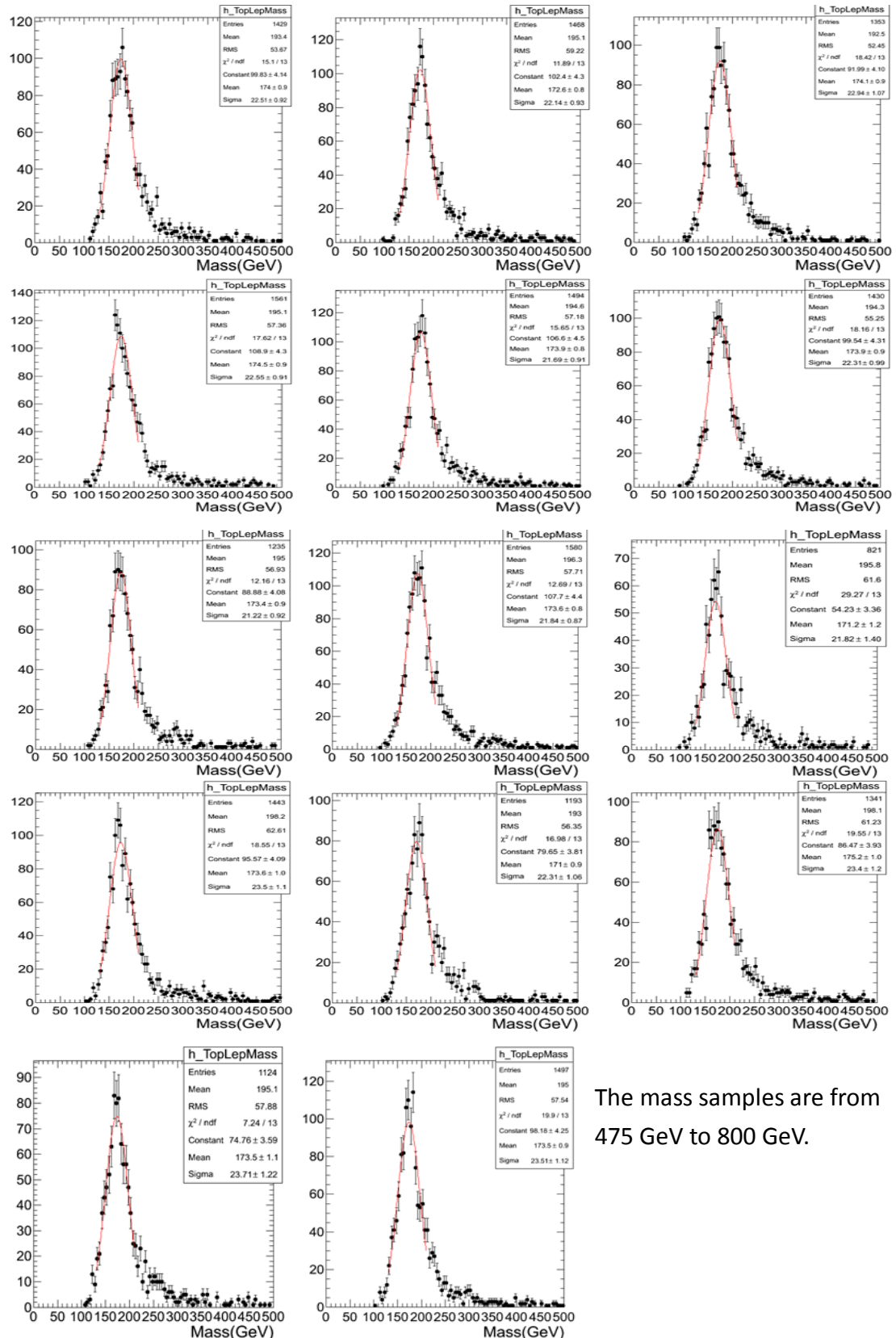
The mass samples are
from 475 GeV to 800 GeV.

A-5 Hadronic t^* Mass Resolution



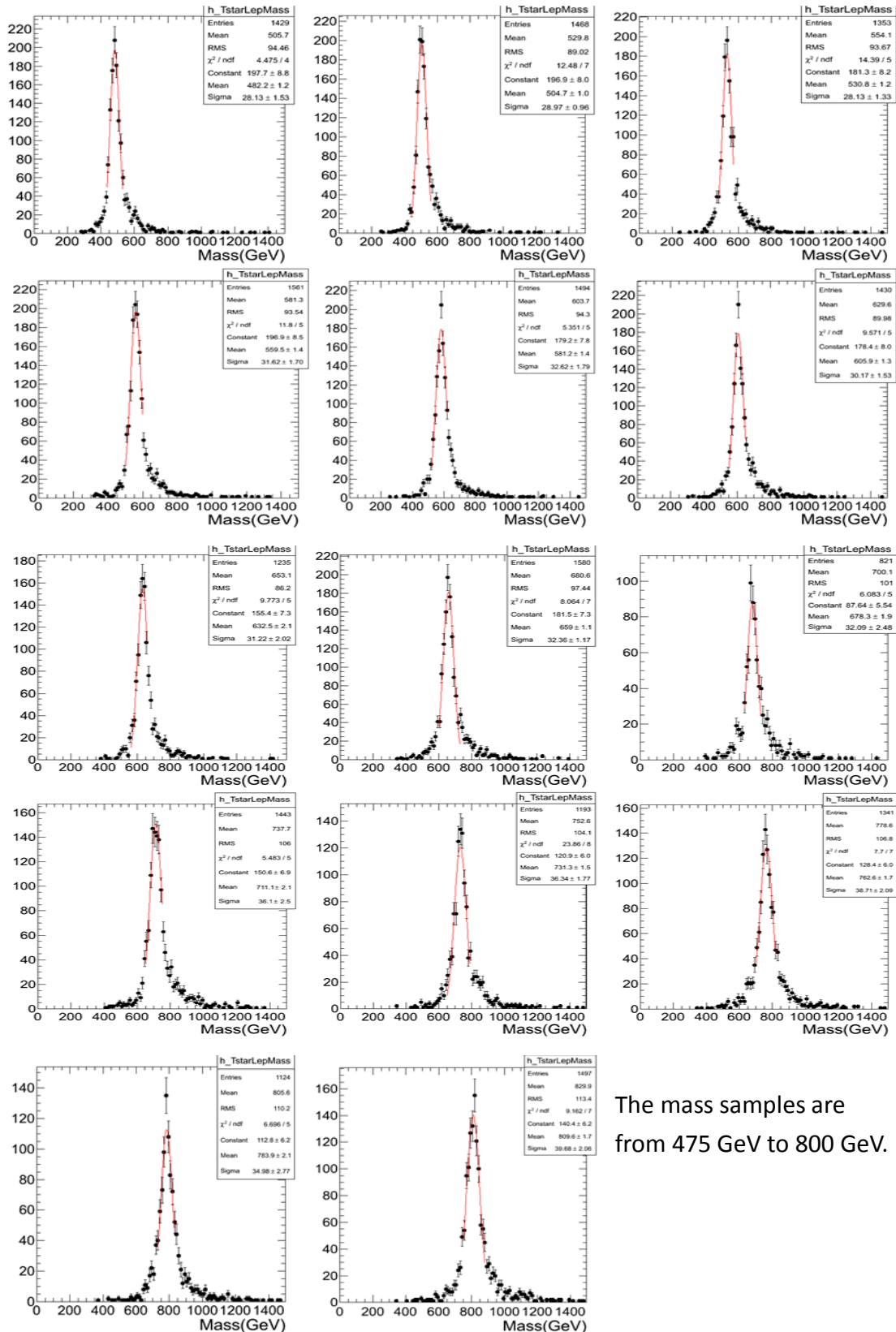
The mass samples are
from 475 GeV to 800 GeV.

A-6 Leptonic top Mass Resolution



The mass samples are from
475 GeV to 800 GeV.

A-7 Leptonic t^* Mass Resolution



The mass samples are
from 475 GeV to 800 GeV.

Reference

- [1] CPEP Contemporary Physics Education Project.
- [2] T. Kaluza, Sitzungsber. Preuss. Akad. Wiss. Berlin (Math. Phys.) **K1**, 966 (1921); O. Klein, Z. Phys. **37**, 895 (1926).
- [3] J. Polchinski, String Theory, Cambridge, Vol. I, chap. 8: Toroidal compactification and T-duality (1995).
- [4] L. Randall and R. Sundrum, Phys. Rev. Lett. **83**, 3370 (1999) [arXiv: hep-ph/9905221]; Phys. Rev. Lett. **83**, 4690 (1999) [arXiv: hep-th/9906064].
- [5] T. Gherghetta and A. Pomarol, Nucl. Phys. B **586**, 141 (2000) [arXiv: hep-ph/0003129].
- [6] Copyright 2005 The New York Times Company.
- [7] S. B. Giddings, S. Kachru and J. Polchinski, Phys. Rev. D **66** (2002) 106006 [arXiv: hep-th/0105097].
- [8] Physics searches at the LHC. arXiv: 0912.3259 [hep-ph] 4 Sep 2010.
- [9] Maxime Gabella. The Randall-Sundrum Model. June 2006 IPPC, EPFL.
- [10] Babiker Hassanain, John March-Russell and J. G. Rosa, “On the possibility of light string resonances at the LHC and Tevatron from Randall-Sundrum throats”[arXiv: 0904.4108v2]
- [11] P. W. Higgs, “Broken symmetries and the masses of gauge bosons,” Phys. Rev. Lett., vol. 13, pp. 508-509, Oct 1964. 1.1
- [12] P. Higgs, “Broken symmetries, massless particles and gauge fields,” Physics Letters, vol. 12, no. 2, pp. 132-133, 1964. 1.1
- [13] CERN, “The CERN accelerator complex.”
<http://public.web.cern.ch/public/en/research/AccelComplex-en.html,2012>.
- [14] The CMS Collaboration, “The CMS experiment at the CERN LHC,” Journal of Instrumentation, vol. 3, 2008. 2.2
- [15] G. Bayatian et al., “CMS Physics Technical Design Report Volume I: Detector Performance and Software,” Technical Design Report CMS, 2006.
- [16] The CMS Collaboration, The CMS tracker system project: Technical Design Report. Technical Design Report CMS, Geneva: CERN, 1997. 2.2.3
- [17] The CMS Collaboration, The CMS tracker: addendum to the Technical Design Report. Technical Design Report CMS, Geneva: CERN, 2000. 2.2.3
- [18] The CMS ECAL: Technical Design Report. Technical Design Report, Geneva: CERN, December 1997. 2.2.4
- [19] P. Bloch, R. Brown, P. Lecoq, and H. Rykaczewski, Changes to CMS ECAL electronics: addendum to the Technical Design Report. Technical Design Report CMS, Geneva:

CERN, 2002. 2.2.4

- [20] CMS Collaboration, CERN/LHCC 20-016(2006), CMS TDR 8.1
- [21] The CMS Collaboration, The CMS hadron calorimeter project: Technical Design Report. Technical Design Report CMS, Geneva: CERN, 1997. 2.2.5
- [22] J. Damgov and S. Kunori, private communication
- [23] Efe Yazgan, Thesis, Department of Physics, Middle East Technical University (2007)
- [24] The CMS Collaboration, The CMS muon project: Technical Design Report. Technical Design Report CMS, Geneva: CERN, 1997 2.2.6
- [25] C. D. Jonew et al., “The new CMS data model and framework,” in CHEP’06 Conference Proceedings. 2006.
- [26] T. Sjostrand, S. Mrenna and P. Skands, “PYTHIA 6.4 Physics and Manual,” *JHEP* **0605** (2006).
- [27] S. Agostinelli et al., “Geant4- A Simulation Toolkit,” *Nuclear Instruments and Methods A* **506** (2003).
- [28] S. Agostinelli et al., GEANT4: A simulation toolkit, *Instrum. and Methods*, A506:250-303, 2003.
- [29] S. Abdullin et al., “The Fast Simulation of the CMS Detector at LHC,” *CMS Conference Report* **297** (2010).
- [30] E. Meschi et al., Electron Reconstruction in the CMS Electromagnetic. Calorimeter, *CMS Note* 2001/034.
- [31] P. Fayet, *Nucl. Phys. B* **90**, 104 (1975).
- [32] N. Marinelli. *CMS Note*, 2006/005, 2006/
- [33] Marinelli N., Kolberg T., Jessop C., Ruchti, R. *CMS Analysis Note*, 2008/102, 2008.
- [34] The CMS Collaboration. *CMS Physics Analysis Summary*, 2010/005, 2010.
- [35] W. Adam, R. Fruhwirth, A. Strandlie, T. Todorov, Reconstruction of electrons with the Gaussian-sum filter in the CMS tracker at the LHC, *J. Phys. G: Nucl. Part. Phys.* **31** (2005) N9-N20.
- [36] C. Charlot, C. Rovelli, Y. Sirois, Reconstruction of Electron Tracks Using Gaussian Sum Filter in CMS, *CMS Analysis Note AN-2005-011* (2006).
- [37] M. Cacciari, G. P. Salam, and G. Soyez, “The Anti- $k(t)$ jet clustering algorithm,” *JHEP* 0804 (2008) 063, arXiv: 0802.1189 [hep-ph].
- [38] J. Alwall, P. Demin, S. de Visscher, R. Frederix, M. Herquet, et al., “MadGraph/MadEvent v4: The New Web Generation,” *JHEP* **0709** (2007) 028, arXiv: 0706.2334 [hep-ph].
- [39] S. Frixion, P. Nason, and G. Ridolfi, “A Positive-weight next-to-leading-order Monte Carlo for heavy flavor hadroproduction,” *JHEP* **0709** (2007) 126.
- [40] S. Alioli, P. Nason, C. Oleari, and E. Re, “NLO single-top production matched with

shower in POWHEG: s- and t-channel contributions,” JHEP **0909** (2009) 111, arXiv: 0907.4076 [hep-ph].

[41] E. Re, “Single-top Wt-channel production matched with parton showers using the POWHEG method,” Eur.Phys.J. **C71** (2011) 1547, arXiv: 1009. 2450 [hep-ph].

[42] R. and Fruhwirth. Application of kalman _ltering to track and vertex _tting. <http://www.sciencedirect.com/science/article/pii/0168900287908874>, 1987.